Université de Montréal

Estimation de cartes d'énergie de hautes fréquences ou d'irrégularité de périodicité de la marche humaine par caméra de profondeur pour la détection de pathologies

par

Didier Ndayikengurukiye

Département d'informatique et de recherche opérationnelle
Faculté des arts et des sciences

Mémoire présenté à la Faculté des arts et des sciences
en vue de l'obtention du grade de Maître ès sciences (M.Sc.)
en informatique

Avril, 2016

RÉSUMÉ

Ce travail présente deux nouveaux systèmes simples d'analyse de la marche humaine grâce à une caméra de profondeur (Microsoft Kinect ^{TM}) placée devant un sujet marchant sur un tapis roulant conventionnel, capables de détecter une marche saine et celle déficiente. Le premier système repose sur le fait qu'une marche normale présente typiquement un signal de profondeur lisse au niveau de chaque pixel avec moins de hautes fréquences, ce qui permet d'estimer une carte indiquant l'emplacement et l'amplitude de l'énergie de haute fréquence (HFSE). Le second système analyse les parties du corps qui ont un motif de mouvement irrégulier, en termes de périodicité, lors de la marche. Nous supposons que la marche d'un sujet sain présente partout dans le corps, pendant les cycles de marche, un signal de profondeur avec un motif périodique sans bruit. Nous estimons, à partir de la séquence vidéo de chaque sujet, une carte montrant les zones d'irrégularités de la marche (également appelées énergie de bruit apériodique). La carte avec HFSE ou celle visualisant l'énergie de bruit apériodique peut être utilisée comme un bon indicateur d'une éventuelle pathologie, dans un outil de diagnostic précoce, rapide et fiable, ou permettre de fournir des informations sur la présence et l'étendue de la maladie ou des problèmes (orthopédiques, musculaires ou neurologiques) du patient. Même si les cartes obtenues sont informatives et très discriminantes pour une classification visuelle directe, même pour un non-spécialiste, les systèmes proposés permettent de détecter automatiquement les individus en bonne santé et ceux avec des problèmes locomoteurs.

Mots clés: Analyse clinique de la marche, bruit apériodique, énergie spectrale haute fréquence, classification de la marche, capteur de profondeur Kinect, mouvement périodique de la marche.

ABSTRACT

This work presents two new and simple human gait analysis systems based on a depth camera (Microsoft Kinect^{TM}) placed in front of a subject walking on a conventional treadmill, capable of detecting a healthy gait from an impaired one. The first system presented relies on the fact that a normal walk typically exhibits a smooth motion (depth) signal, at each pixel with less high-frequency spectral energy content than an abnormal walk. This permits to estimate a map for that subject, showing the location and the amplitude of the high-frequency spectral energy (HFSE). The second system analyses the patient's body parts that have an irregular movement pattern, in terms of periodicity, during walking. Herein we assume that the gait of a healthy subject exhibits anywhere in the human body, during the walking cycles, a depth signal with a periodic pattern without noise. From each subject's video sequence, we estimate a saliency color map showing the areas of strong gait irregularities also called aperiodic noise energy. Either the HFSE or aperiodic noise energy shown in the map can be used as a good indicator of possible pathology in an early, fast and reliable diagnostic tool or to provide information about the presence and extent of disease or (orthopedic, muscular or neurological) patient's problems. Even if the maps obtained are informative and highly discriminant for a direct visual classification, even for a non-specialist, the proposed systems allow us to automatically detect maps representing healthy individuals and those representing individuals with locomotor problems.

Keywords: Clinical gait analysis, aperiodic noise, spectral energy, asymmetry gait or swing, noise aperiodicity, gait classification, Kinect depth sensor, periodic gait motion.

TABLE DES MATIÈRES

LISTE DES FIGURES

LISTE DES TABLEAUX

LISTE DES ALGORITHMES

LISTE DES SIGLES

2D	2 dimensions
3D	3 dimensions
DAG	directed acyclic graph
DEI	depth energy image
DIRO	département d'informatique et de recherche opérationnelle
EMG	électromyographie
GNB	gaussian naive bayes
HFSE	high-frequency spectral energy
Hz	unité du système international de mesure de la fréquence, hertz
IR	infrared
k-NN	k-nearest neighbors
k-PPV	k plus proches voisins
LLD	length leg discrepancy
LOOCV	leave one out cross-validation
LR	logistic regression
NB	naive bayes
PCA	principal component analysis
S15	individu numéro 15
SGD	stochastic gradient descent
SGDC	stochastic gradient descent classifier
SVM	séparateurs à vastes marges ou machines à vecteurs de support ou "support vector machine"
TM	trade mark
TOF	time-of-flight

NOTATION

$AS(I)$	(asymétrie) déformation de la silhouette de la carte I
	de l'énergie du bruit apériodique
cf.	confer
Fig.	figure
$\mathbf{x} = \begin{pmatrix} x_1 \\ \vdots \\ x_d \end{pmatrix}$	vecteur
$\|\mathbf{x}\|_2$	norme euclidienne du vecteur $\mathbf{x}$
$\mathbf{z}_i = (\mathbf{x}_i, y_i)$	élément d'un échantillon d'apprentissage
$\mathbf{x}_i$	description d'un objet dans un espace de représentation
y_i	sortie de $\mathbf{x}_i$
x_{ij}	valeur de la coordonnée j de $\mathbf{x}_i$
$\mathbf{w}$	vecteur poids
w_0	biais
$\frac{\partial f(x,\ldots,y)}{\partial x}$	dérivée partielle par rapport à x de la fonction f des variables x, ... et y
$\langle \mathbf{x}, \mathbf{y} \rangle$	produit intérieur (ou produit scalaire) entre $\mathbf{x}$ et $\mathbf{y}$
$\Phi(\mathbf{x})$	vecteur de fonctions $\phi_i(\mathbf{x})$ de transformation de l'espace de $\mathbf{x}$ vers un autre espace
$\phi_i(\mathbf{x})$	fonction de transformation de $\mathbf{x}$
χ	espace de coordonnées
$K(\mathbf{x}, \mathbf{y})$	noyau $\langle \Phi(\mathbf{x}), \Phi(\mathbf{y}) \rangle$
$\mathbf{X}$	matrice
X_{ij}	élément de la matrice
$p(x)$	une densité de probabilité suivant laquelle se distribue x
$L(\mathbf{w}, w_0, \alpha)$	le lagrangien
$\mathbb{R}$	ensemble des réels
$\mathbb{R}^d$	espace euclidien de dimension d

À mon épouse, mes enfants, mes parentés,
tous ceux qui m'ont soutenu depuis l'enfance.

REMERCIEMENTS

Je voudrais remercier mon Directeur de recherche, le Professeur Max Mignotte qui a accompli son rôle de superviseur de façon excellente. Il m'a guidé dans l'apprentissage tout au long de ce deuxième cycle universitaire, m'a partagé ses connaissances dans mon domaine d'étude et m'a encouragé dans mes travaux académiques. Mes remerciements sont adressés aussi à tous les Professeurs de l'Université de Montréal spécialement à ceux du département d'informatique et de recherche opérationnelle (DIRO) par qui j'ai eu accès aux connaissances académiques qu'ils dispensent. Je remercie tout le personnel de l'Université de Montréal en particulier celui du département d'informatique et de recherche opérationnelle (DIRO) qui a rendu mes études académiques possibles. Je voudrais aussi remercier mon épouse, mes enfants et toute ma famille pour leur soutien, chacun de sa façon. Je remercie particulièrement mon épouse pour sa patience dans les exigences académiques auxquelles j'ai fait face. Que tous ceux qui m'ont soutenu de près ou de loin trouvent ici ma profonde gratitude.

CHAPITRE 1

INTRODUCTION

La marche et la course sont des activités que l'Homme effectue le plus souvent tout au long de sa vie naturellement et aussi longtemps que son corps ne souffre pas d'handicap. Elles ont fait l'objet de recherche depuis longtemps [1] et continuent même actuellement. Selon Winter, la locomotion humaine, c'est-à-dire la marche et la course, a été décrite et analysée plus que tout autre mouvement total, et beaucoup de laboratoires sont dédiés à son évaluation, à la fois dans le cadre d'une locomotion normale ou pathologique [2].

Mise à part son rôle dans la détection de maladies, la marche humaine peut être utile dans l'identification ou la reconnaissance de personnes [3–5]. De plus, des chercheurs envisagent la marche humaine dans la biométrie, comme un instrument d'authentification à l'instar des empreintes digitales, des yeux (l'iris et la rétine) et le visage, ayant l'avantage de ne pas toujours exiger la proximité de la personne à authentifier [6–8]. L'analyse de la marche humaine est largement utilisée en lien avec la santé humaine et ceci plus que tous les autres domaines. Cette analyse nécessite des mesures et des techniques pour effectuer ces mesures. Ces dernières varient en fonction de l'orientation, des intérêts et des outils des chercheurs. Pour les chercheurs orientés "clinique", ce sont surtout les mesures observables visuellement sur le patient qui sont intéressantes : la longueur de la foulée, la cadence et les angles des articulations. Les chercheurs orientés "neurologique" se focalisent sur les mesures électromyographiques (EMG) tandis que les chercheurs en biomécanique analysent surtout la cinématique, les forces de réaction, les moments de forces, les puissances et les énergies. Certaines de ces mesures sont essentiellement liées aux causes (signaux EMG), d'autres aux effets (la longueur de la foulée) d'une marche normale ou pathologique [2].

Dans ce travail, nous nous sommes intéressé d'une part, aux mesures de l'énergie de haute fréquence (HFSE) et d'autre part, à la mesure de l'irrégularité de périodicité de la marche humaine. Nous verrons que ces deux mesures sont particulièrement discri-

minantes pour pouvoir classer ensuite la marche d'un individu sain et celle associée à un individu souffrant d'un problème locomoteur. Ces mesures ont été effectuées sur 17 individus, chacun effectuant sur un tapis roulant conventionnel une marche normale (A), puis une marche avec une talonnette à la jambe gauche (B) et finalement une marche avec une talonnette à la jambe droite (C). Il ressort de ce qui précède que le nombre total de nos vidéos de profondeur est 51, vidéos acquises grâce à une caméra de profondeur (Microsoft Kinect^{TM}). La visualisation en fausse couleur du résultat de ces deux mesures (localisation et amplitude) sur une carte, représentant l'individu durant son cycle de marche, peut aider les cliniciens dans leurs diagnostics. De plus, nous estimons que ces cartes peuvent aussi faciliter la détection des maladies neurologiques dans la mesure où les anomalies pourront être localisées sur la carte du corps du patient. Bien que les cartes obtenues soient informatives et très discriminantes pour une classification visuelle directe, même pour un non-spécialiste, nous nous sommes intéressé aussi à définir des algorithmes de détection automatique des individus en bonne santé et de ceux avec des problèmes locomoteurs. Pour ce faire, nous avons eu recours à l'apprentissage automatique. Les modèles de classification utilisés dans cet apprentissage sont : les machines à vecteurs de support (SVM), le modèle gaussien de Bayes naïf, le modèle multinoulli de Bayes naïf, le k-plus-proches-voisins, k-PPV (k-NN), la régression logistique (LR). Nous avons aussi utilisé les techniques comme le gradient stochastique descendant (SGD) et la validation croisée dont on peut trouver les détails dans les chapitres qui suivent.

BIBLIOGRAPHIE

[1] Reinhard Klette and Garry Tee. Understanding human motion : A historic review. *3d Imaging for Safety and Security*, 1 :22–40, 2007.

[2] David A Winter. *Biomechanics and motor control of human gait : normal, elderly and pathological*. 1991.

[3] Ross Cutler and Larry S Davis. Robust real-time periodic motion detection, analysis, and applications. *IEEE Transactions on Pattern Analysis and Machine Intelligence*, 22(8) :781–796, 2000.

[4] Robert T Collins, Ralph Gross, and Jianbo Shi. Silhouette-based human identification from body shape and gait. In *Proceedings. Fifth IEEE International Conference on Automatic Face and Gesture Recognition, 2002*, pages 366–371. IEEE, 2002.

[5] Amit Kale, AN Rajagopalan, Naresh Cuntoor, and Volker Kruger. Gait-based recognition of humans using continuous hmms. In *Proceedings. Fifth IEEE International Conference on Automatic Face and Gesture Recognition, 2002*, pages 336–341. IEEE, 2002.

[6] Philippe Claude Cattin. *Biometric authentication system using human gait*. PhD thesis, Citeseer, 2002.

[7] P Jonathon Phillips, Sudeep Sarkar, Isidro Robledo, Patrick Grother, and Kevin Bowyer. Baseline results for the challenge problem of humanid using gait analysis. In *Proceedings. Fifth IEEE International Conference on Automatic Face and Gesture Recognition, 2002*, pages 130–135. IEEE, 2002.

[8] Jamie D Shutler, Michael G Grant, Mark S Nixon, and John N Carter. On a large sequence-based human gait database. In *Applications and Science in Soft Computing*, pages 339–346. Springer, 2004.

CHAPITRE 2

TECHNIQUES UTILISÉES DANS NOTRE CLASSIFICATION DE PATIENTS

2.1 Machines à Vecteurs de Support (SVM)

Les SVM ont été inventés par Boser, Guyon et Vapnik et introduits dans leur article [1]. Toutefois, la plupart des théories qui y sont reliées ont été présentées et utilisées en apprentissage machine dès les années 1960 [2]. Les SVM sont l'un des outils les plus utilisés pour l'apprentissage machine.

2.1.1 Séparateur à Marge Maximale ou SVM avec Marge Rigide (Hard Margin SVM)

Pour expliquer cette technique, partons du cas de classification en deux classes de points $\mathbf{x}_i \in \mathbb{R}^d$, linéairement séparables (cf. Fig. 2.1). Soient les exemples d'apprentissage $(\mathbf{x}_1, y_1), (\mathbf{x}_2, y_2), ..., (\mathbf{x}_m, y_m)$ et $y_i \in \{-1, 1\}$ (y_i étant les étiquettes des deux classes). Le SVM cherche un hyperplan optimal qui sépare les points en question. Nous faisons l'hypothèse qu'il existe un hyperplan d'équation $h(\mathbf{x}) = \langle \mathbf{w}, \mathbf{x} \rangle + w_0$ qui sépare ces deux classes avec $\mathbf{w} \in \mathbb{R}^d$ et $w_0 \in \mathbb{R}$, $\mathbf{w}$ étant son vecteur normal. La fonction de décision pour cette classification est alors :

$$f(\mathbf{x}) = \text{sign}(\langle \mathbf{w}, \mathbf{x} \rangle + w_0) \tag{2.1}$$

Cet hyperplan va faire une bonne classification de tous les exemples d'apprentissage si $\forall\, 1 \leq i \leq m,\ y_i(\langle \mathbf{w}, \mathbf{x}_i \rangle + w_0) > 0$. La fonction $y_i(\langle \mathbf{w}, \mathbf{x}_i \rangle + w_0)$ est appelée la marge fonctionnelle de l'exemple $(\mathbf{x}_i, y_i)$ par rapport à l'hyperplan $(\mathbf{w}, w_0)$. La marge géométrique est égale à $\frac{y_i(\langle \mathbf{w}, \mathbf{x}_i \rangle + w_0)}{\|\mathbf{w}\|_2}$. Or pour un scalaire $\lambda \geq 0$ avec $\mathbf{w}' = \lambda \mathbf{w}$ et $w'_0 = \lambda w_0$, la marge

géométrique sera alors égale à :

$$\begin{aligned}
&\frac{y_i(\langle \mathbf{w}', \mathbf{x}_i \rangle + w_0')}{\|\mathbf{w}'\|} = \frac{y_i(\langle \lambda \mathbf{w}, \mathbf{x}_i \rangle + \lambda w_0)}{\|\lambda \mathbf{w}\|_2} \\
&= \frac{\lambda y_i(\langle \mathbf{w}, \mathbf{x}_i \rangle + w_0)}{|\lambda| \, \|\mathbf{w}\|_2} \\
&= \frac{\lambda y_i(\langle \mathbf{w}, \mathbf{x}_i \rangle + w_0)}{\lambda \, \|\mathbf{w}\|_2} \\
&= \frac{y_i(\langle \mathbf{w}, \mathbf{x}_i \rangle + w_0)}{\|\mathbf{w}\|_2}
\end{aligned}$$

Nous voyons que la multiplication par un scalaire $\lambda > 0$ des paramètres $\mathbf{w}$ et w_0 n'a pas changé la marge géométrique de l'exemple $(\mathbf{x}_i, y_i)$. Nous pouvons donc chercher un $\mathbf{w}$ tel que la marge fonctionnelle soit égale à 1 et la marge géométrique devenant $\frac{1}{\|\mathbf{w}\|_2}$.

La marge fonctionnelle de l'ensemble d'apprentissage par rapport à un hyperplan est la plus petite marge fonctionnelle des exemples d'apprentissage par rapport à cet hyperplan. La marge de l'ensemble d'entraînement est la marge géométrique maximale de tous les hyperplans. L'hyperplan pour qui on a obtenu cette marge géométrique maximale est appelé *hyperplan à marge maximale* [2].

Nous pouvons donc trouver le séparateur à marge maximale (ou l'hyperplan optimal) en maximisant la marge géométrique ($\frac{1}{\|\mathbf{w}\|_2}$) ce qui revient à minimiser $\langle \mathbf{w}, \mathbf{w} \rangle$. Comme nous maximisons cette distance de part et d'autre de l'hyperplan, la marge à maximiser sera alors $\frac{2}{\|\mathbf{w}\|_2}$ et par conséquent nous minimisons $\frac{1}{2}\langle \mathbf{w}, \mathbf{w} \rangle$. Le problème d'optimisation à résoudre est [2–4]. :

$$\begin{cases} \text{minimiser } \frac{1}{2}\langle \mathbf{w}, \mathbf{w} \rangle \textit{ sur } \mathbf{w} \in \mathbb{R}^d \\ \text{sous les contraintes : } y_i(\langle \mathbf{w}, \mathbf{x}_i \rangle + w_0) \geq 1, \ i = 1, ..., m \textit{ et } w_0 \in \mathbb{R} \end{cases} \tag{2.2}$$

Cette technique est aussi appelée SVM avec marge rigide à cause des contraintes $y_i(\langle \mathbf{w}, \mathbf{x}_i \rangle + w_0) \geq 1$ avec $i = 1, ..., m$, qui obligent les hyperplans à ne pas faire d'erreurs sur les données d'entraînement.

Pour des points $\mathbf{x}_i$ de l'espace des entrées χ ($\chi = \mathbb{R}^d$ dans notre cas) et qui sont non-linéairement séparables, on utilise une transformation non linéaire Φ qui va rendre les $\Phi(\mathbf{x}_i)$ linéairement séparables dans $\Phi(\chi)$.

$$\mathbf{x}_i = (x_{1i}, ..., x_{di})^T \mapsto \Phi(\mathbf{x}_i) = (\phi_1(\mathbf{x}_i), ..., \phi_d(\mathbf{x}_i)) \tag{2.3}$$

$$\begin{cases} \text{minimiser } \frac{1}{2}\langle \mathbf{w}, \mathbf{w} \rangle \; sur \; \mathbf{w} \in \Phi(\chi) \\ \text{sous les contraintes : } y_i(\langle \mathbf{w}, \Phi(\mathbf{x}_i) \rangle + w_0) \geq 1, \;\; i = 1, ..., m \; et \; w_0 \in \mathbb{R} \end{cases} \tag{2.4}$$

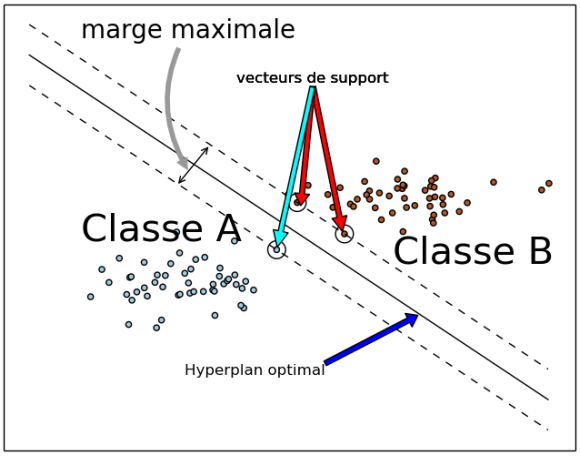

FIGURE 2.1: Hyperplan optimal et vecteurs de support obtenus avec le SVM à marge rigide pour deux classes A et B de points linéairement séparables (pour la dimension d=2).

2.1.2 SVM avec Marge Molle (Soft Margin SVM)

En présence de bruits, pour faire la meilleure classification possible, on ajoute des variables $\xi \in \mathbb{R}^m$, appelées variables ressort ("slack variables"), avec $\xi_i \geq 0$ telles que $y_i(\langle \mathbf{w}, \mathbf{x}_i \rangle) + w_0) \geq 1 - \xi_i$. Ceci parce que les contraintes : $y_i(\langle \mathbf{w}, \mathbf{x}_i \rangle) + w_0) \geq 1$ forcent les hyperplans à ne pas faire d'erreurs dans la séparation des données d'entraînement

(cf. la section 2.1.1). On ajoute une pénalité à la fonction objective et on modifie les contraintes en les relâchant par des variables ressorts.

De plus, dans les cas où on ne parvient pas à obtenir une transformation Φ pouvant aboutir à des points linéairement séparables dans le nouvel espace, on peut recourir aux SVM avec marge molle. Le problème d'optimisation est alors :

$$\begin{cases} \text{minimiser } \frac{1}{2}\langle \mathbf{w}, \mathbf{w} \rangle + C \sum_{i=1}^{m} \xi_i \text{ sur } \mathbf{w} \in \Phi(\chi) \text{ et } C > 0 \\ \text{sous les contraintes : } \begin{cases} y_i(\langle \mathbf{w}, \Phi(\mathbf{x}_i) \rangle + w_0) \geq 1 - \xi_i, \ i = 1, ..., m \text{ et } w_0 \in \mathbb{R} \\ \xi_i \geq 0, \ i = 1, ..., m \end{cases} \end{cases} \tag{2.5}$$

2.1.3 Formulation Duale du Problème de SVM

Les problèmes d'optimisation présentés dans les sections 2.1.1 et 2.1.2 (dits aussi de formulation primale) sont des problèmes d'optimisation convexe [2]. Leur traitement par la méthode de Lagrange les rend facile à résoudre car c'est difficile de gérer directement les contraintes surtout quand la dimension des entrées devient grande [2, 3].

Soient le lagrangien $L(\mathbf{w}, w_0, \alpha)$ (α_i, $i = 1, ...m$, étant les multiplicateurs de Lagrange, $\alpha_i \geq 0$). Pour chacun des problèmes de formulation primale des sections précédentes, la solution est le point où les dérivées partielles du lagrangien qui lui est associé s'annulent (point-selle).

2.1.3.1 Formulation duale pour SVM avec marge rigide

Le lagrangien correspondant au SVM avec marge rigide (séparateur à marge maximale) est :

$$L(\mathbf{w}, w_0, \alpha) = \frac{1}{2}\langle \mathbf{w}, \mathbf{w} \rangle - \sum_{i=1}^{m} \alpha_i (y_i.(\langle \mathbf{w}, \Phi(\mathbf{x}_i) \rangle + w_0) - 1) \ \textit{avec } \alpha_i \geq 0 \tag{2.6}$$

Nous aurons donc le système d'équations :

$$\begin{cases} \frac{\partial L(\mathbf{w},w_0,\alpha)}{\partial \mathbf{w}} = \mathbf{w} - \sum_{i=1}^{m} \alpha_i y_i \Phi(\ \mathbf{x}_i) \\ \frac{\partial L(\mathbf{w},w_0,\alpha)}{\partial w_0} = \sum_{i=1}^{m} \alpha_i y_i \end{cases} \tag{2.7}$$

Comme les dérivées partielles doivent s'annuler :

$$\begin{cases} \frac{\partial L(\mathbf{w},w_0,\alpha)}{\partial \mathbf{w}} = 0 \\ \frac{\partial L(\mathbf{w},w_0,\alpha)}{\partial w_0} = 0 \end{cases} \tag{2.8}$$

Le système d'équations devient :

$$\begin{cases} \mathbf{w} - \sum_{i=1}^{m} \alpha_i y_i \Phi(\ \mathbf{x}_i) = 0 \\ \sum_{i=1}^{m} \alpha_i y_i = 0 \end{cases} \tag{2.9}$$

Ce qui donne finalement le système :

$$\begin{cases} \mathbf{w} = \sum_{i=1}^{m} \alpha_i y_i \Phi(\ \mathbf{x}_i) \\ \sum_{i=1}^{m} \alpha_i y_i = 0 \end{cases} \tag{2.10}$$

En remplaçant les valeurs 2.10 dans 2.6 nous obtenons :

$$L(\mathbf{w},w_0,\alpha) = \frac{1}{2}\langle \mathbf{w},\mathbf{w}\rangle - \sum_{i=1}^{m} \alpha_i (y_i.(\langle \mathbf{w}, \Phi(\mathbf{x}_i)\rangle + w_0) - 1) \tag{2.11}$$

$$= \frac{1}{2}\sum_{i,j=1}^{m} \alpha_i \alpha_j y_i y_j \langle \Phi(\mathbf{x}_i), \Phi(\mathbf{x}_j)\rangle - \sum_{i,j=1}^{m} \alpha_i \alpha_j y_i y_j \langle \Phi(\mathbf{x}_i), \Phi(\mathbf{x}_j)\rangle + \sum_{i,j=1}^{m} \alpha_i \tag{2.12}$$

$$= \sum_{i,j=1}^{m} \alpha_i - \frac{1}{2}\sum_{i,j=1}^{m} \alpha_i \alpha_j y_i y_j \langle \Phi(\mathbf{x}_i), \Phi(\mathbf{x}_j)\rangle \tag{2.13}$$

La représentation duale du problème d'optimisation est donc :

$$\begin{cases} \max_{\alpha}\{\sum_{i=1}^{m}\alpha_i - \frac{1}{2}\sum_{i,j=1}^{m}\alpha_i\alpha_j y_i y_j \langle\Phi(\mathbf{x}_i),\Phi(\mathbf{x}_j)\rangle\} \\ \alpha_i \geq 0,\ i = 1,...,m \\ \sum_{i=1}^{m}\alpha_i y_i = 0 \end{cases} \tag{2.14}$$

Les solutions à ce problème d'optimisation sont les α_i^*. À partir de 2.10, nous avons :

$$\mathbf{w}^* = \sum_{i=1}^{m}\alpha_i^* y_i \Phi(\ \mathbf{x}_i) \tag{2.15}$$

Pour obtenir w_0^*, nous partons de la condition de Karush-Kuhn-Tucker :

$$\alpha_i^*\,[y_i(\langle\mathbf{w}^*,\Phi(\mathbf{x}_i)\rangle + w_0^*) - 1] = 0 \tag{2.16}$$

Pour les $\alpha_i^* \neq 0$, nous aurons :

$$y_i(\langle\mathbf{w}^*,\Phi(\mathbf{x}_i)\rangle + w_0^*) - 1 = 0 \tag{2.17}$$

$$\Rightarrow\ y_i(\langle\mathbf{w}^*,\Phi(\mathbf{x}_i)\rangle + w_0^*) = 1 \tag{2.18}$$

$\Rightarrow$ les $\Phi(\mathbf{x}_i)$ qui vérifient 2.18 sont les plus proches de l'hyperplan optimal. D'après l'équation 2.15, les $\alpha_i^* = 0$ ne comptent pas dans le calcul de w^*. Soit VS l'ensemble des indices de $\alpha_j^* \neq 0$. L'équation 2.15 s'écrit :

$$\mathbf{w}^* = \sum_{i\in VS}\alpha_i^* y_i \Phi(\ \mathbf{x}_i),\ VS = \{j : \alpha_j^* \neq 0\} \tag{2.19}$$

Ces $\mathbf{x}_i$ pour lesquels $i \in VS$ sont appelés des vecteurs de support. De plus :

$$w_0^* = y_j - \sum_{i=1}^{m}\alpha_i^* y_i \langle\Phi(\mathbf{x}_i),\Phi(\mathbf{x}_j)\rangle,\ j \in VS = \{j : \alpha_j^* \neq 0\} \tag{2.20}$$

Finalement, l'équation de l'hyperplan optimal dans la formulation duale pour SVM avec

marge rigide est :

$$h(\mathbf{x}) = \sum_{i=1}^{m} \alpha_i^* y_i \langle \Phi(\mathbf{x}_i), \Phi(\mathbf{x}) \rangle + w_0^* \tag{2.21}$$

Il faudra noter que dans l'espace non transformé, les résultats sont identiques à part que dans ce cas la transformation $\Phi(\mathbf{x}) = \mathbf{x}$.

2.1.3.2 Formulation duale pour SVM avec marge molle

Pour le SVM avec marge molle, la formulation primale du problème est exprimée par l'équation 2.5. Le lagrangien qui lui est associé est alors :

$$L(\mathbf{w}, w_0, \xi, \alpha, \mathbf{r}) = \frac{1}{2}\langle \mathbf{w}, \mathbf{w} \rangle + C\sum_{i=1}^{m} \xi_i - \sum_{i=1}^{m} \alpha_i (y_i(\langle \mathbf{w}, \Phi(\mathbf{x}_i) \rangle + w_0) - 1 + \xi_i) - \sum_{i=1}^{m} r_i \xi_i \tag{2.22}$$

Avec $\alpha_i \geq 0$ et $r_i \geq 0$ (α_i et r_i sont des multiplicateurs de Lagrange). Nous aurons donc le système d'équations :

$$\begin{cases} \frac{\partial L(\mathbf{w}, w_0, \xi, \alpha, \mathbf{r})}{\partial \mathbf{w}} = \mathbf{w} - \sum\limits_{i=1}^{m} \alpha_i y_i \Phi(\mathbf{x}_i) \\ \frac{\partial L(\mathbf{w}, w_0, \xi, \alpha, \mathbf{r})}{\partial \xi_i} = C - \alpha_i - r_i \\ \frac{\partial L(\mathbf{w}, w_0, \xi, \alpha, \mathbf{r})}{\partial w_0} = \sum\limits_{i=1}^{m} \alpha_i y_i \end{cases} \tag{2.23}$$

Comme les dérivées partielles au point-selle (qui correspond à la solution de la formulation primale) doivent s'annuler, nous aurons :

$$\begin{cases} \mathbf{w} - \sum\limits_{i=1}^{m} \alpha_i y_i \Phi(\mathbf{x}_i) = 0 \\ C - \alpha_i - r_i = 0 \\ \sum\limits_{i=1}^{m} \alpha_i y_i = 0 \end{cases} \tag{2.24}$$

Ce qui donne finalement le système :

$$\begin{cases} \mathbf{w} = \sum_{i=1}^{m} \alpha_i y_i \Phi(\mathbf{x}_i) \\ C - \alpha_i - r_i = 0 \\ \sum_{i=1}^{m} \alpha_i y_i = 0 \end{cases} \tag{2.25}$$

En remplaçant les valeurs 2.25 dans 2.22 nous obtenons :

$$\begin{aligned} & L(\mathbf{w}, w_0, \xi, \alpha, \mathbf{r}) && (2.26) \\ &= \frac{1}{2}\langle \mathbf{w}, \mathbf{w} \rangle + C\sum_{i=1}^{m} \xi_i - \sum_{i=1}^{m} \alpha_i (y_i.(\langle \mathbf{w}, \Phi(\mathbf{x}_i) \rangle + w_0) - 1 + \xi_i) - \sum_{i=1}^{m} r_i \xi_i && (2.27) \\ &= \frac{1}{2}\langle \mathbf{w}, \mathbf{w} \rangle - \sum_{i=1}^{m} \alpha_i (y_i.(\langle \mathbf{w}, \Phi(\mathbf{x}_i) \rangle + w_0) - 1) + \sum_{i=1}^{m} C\xi_i - \sum_{i=1}^{m} (\alpha_i + r_i)\xi_i && (2.28) \\ &= \frac{1}{2}\langle \mathbf{w}, \mathbf{w} \rangle - \sum_{i=1}^{m} \alpha_i (y_i.(\langle \mathbf{w}, \Phi(\mathbf{x}_i) \rangle + w_0) - 1) + \sum_{i=1}^{m} (C - (\alpha_i + r_i))\xi_i && (2.29) \\ &= \frac{1}{2}\langle \mathbf{w}, \mathbf{w} \rangle - \sum_{i=1}^{m} \alpha_i (y_i.(\langle \mathbf{w}, \Phi(\mathbf{x}_i) \rangle + w_0) - 1) + \sum_{i=1}^{m} (C - \alpha_i - r_i))\xi_i && (2.30) \\ &= \frac{1}{2}\langle \mathbf{w}, \mathbf{w} \rangle - \sum_{i=1}^{m} \alpha_i (y_i.(\langle \mathbf{w}, \Phi(\mathbf{x}_i) \rangle + w_0) - 1) && (2.31) \\ &= \frac{1}{2}\sum_{i,j=1}^{m} \alpha_i \alpha_j y_i y_j \langle \Phi(\mathbf{x}_i), \Phi(\mathbf{x}_j) \rangle - \sum_{i,j=1}^{m} \alpha_i \alpha_j y_i y_j \langle \Phi(\mathbf{x}_i), \Phi(\mathbf{x}_j) \rangle + \sum_{i,j=1}^{m} \alpha_i && (2.32) \\ &= \sum_{i,j=1}^{m} \alpha_i - \frac{1}{2}\sum_{i,j=1}^{m} \alpha_i \alpha_j y_i y_j \langle \Phi(\mathbf{x}_i), \Phi(\mathbf{x}_j) \rangle && (2.33) \end{aligned}$$

De plus,

$$\begin{cases} C - \alpha_i - r_i = 0 \\ r_i \geq 0 \end{cases} \tag{2.34}$$

$\Rightarrow C - \alpha_i \geq 0$

$\Rightarrow C \geq \alpha_i$

La représentation duale du problème d'optimisation pour SVM molle et SVM rigide est la même sauf que les contraintes $\alpha_i \geq 0$ deviennent $0 \leq \alpha_i \leq C$, $i = 1, ..., m$. Ceci donne :

$$\begin{cases} \max_\alpha \{ \sum_{i=1}^{m} \alpha_i - \frac{1}{2} \sum_{i,j=1}^{m} \alpha_i \alpha_j y_i y_j \langle \Phi(\mathbf{x}_i), \Phi(\mathbf{x}_j) \rangle \} \\ \forall i \; 0 \leq \alpha_i \leq C, \; i = 1, ..., m \\ \sum_{i=1}^{m} \alpha_i y_i = 0 \end{cases} \tag{2.35}$$

Les solutions à ce problème d'optimisation sont les α_i^*. À partir de 2.25, nous avons :

$$\mathbf{w}^* = \sum_{i=1}^{m} \alpha_i^* y_i \Phi(\mathbf{x}_i) \tag{2.36}$$

Les conditions de Karush-Kuhn-Tucker sont :

$$\alpha_i^* \left[y_i (\langle \mathbf{w}^*, \Phi(\mathbf{x}_i) \rangle + w_0^*) - 1 + \xi_i \right] = 0 \tag{2.37}$$

$$\xi_i (\alpha_i - C) = 0 \tag{2.38}$$

Avec $i = 1, ..., m$.

Pour les $\alpha_i^* \neq 0$, nous aurons, d'après l'équation 2.37 :

$$y_i (\langle \mathbf{w}^*, \Phi(\mathbf{x}_i) \rangle + w_0^*) - 1 + \xi_i = 0 \tag{2.39}$$

$$\Rightarrow \; y_i (\langle \mathbf{w}^*, \Phi(\mathbf{x}_i) \rangle + w_0^*) = 1 - \xi_i \tag{2.40}$$

Or, selon l'équation 2.38, pour les $\xi_i \neq 0$, $C = \alpha_i$. Donc pour les α_i tels que $0 < \alpha_i < C$, l'équation 2.40 donne :

$$y_i (\langle \mathbf{w}^*, \Phi(\mathbf{x}_i) \rangle + w_0^*) = 1 \tag{2.41}$$

$$\Rightarrow w_0^* = y_j - \sum_{i=1}^{m} \alpha_i^* y_i \langle \Phi(\mathbf{x}_i), \Phi(\mathbf{x}_j) \rangle,\ j \in \{ j : 0 < \alpha_j^* < C \} \tag{2.42}$$

Pour le SVM avec marge molle, les vecteurs de support x_i sont donnés par les $\Phi(\mathbf{x}_i)$ pour lesquels les indices sont tels que $0 < \alpha_i < C$.

L'hyperplan optimal est :

$$h(\mathbf{x}) = \langle \mathbf{w}^*, \Phi(\mathbf{x}) \rangle + w_0^* \tag{2.43}$$

Les équations 2.36 et 2.43 donnent :

$$h(\mathbf{x}) = \sum_{i=1}^{m} \alpha_i^* y_i \langle \Phi(\mathbf{x}_i), \Phi(\mathbf{x}) \rangle + w_0^* \tag{2.44}$$

2.1.4 Fonction Noyau pour SVM

L'un des grands avantages de la formulation duale est qu'elle permet l'utilisation des fonctions noyau. Ces dernières facilitent l'utilisation des transformations Φ de façon implicite grâce au procédé appelé "truc du noyau" par lequel les produits scalaires $\langle \Phi(\mathbf{x}), \Phi(\mathbf{y}) \rangle$ dans les formulations des problèmes sont remplacés par les $K(\mathbf{x}, \mathbf{y})$ (K étant une fonction noyau ou "Kernel function" en Anglais). Les fonctions noyau sont des fonctions bilinéaires symétriques positives.

En remplaçant le produit scalaire $\langle \Phi(\mathbf{x}_i), \Phi(\mathbf{x}_j) \rangle$ par la fonction noyau $K(\mathbf{x}_i, \mathbf{x}_j)$, le problème d'optimisation pour le SVM à marge rigide devient :

$$\begin{cases} \max_\alpha \{ \sum\limits_{i=1}^{m} \alpha_i - \frac{1}{2} \sum\limits_{i,j=1}^{m} \alpha_i \alpha_j y_i y_j K(\mathbf{x}_i, \mathbf{x}_j) \} \\ \alpha_i \geq 0,\ i = 1, ..., m \\ \sum\limits_{i=1}^{m} \alpha_i y_i = 0 \end{cases} \tag{2.45}$$

Et l'hyperplan optimal correspondant est :

$$h(\mathbf{x}) = \sum_{i=1}^{m} \alpha_i^* y_i K(\mathbf{x}, \mathbf{x}_i) + w_0^*$$
$$avec\ w_0^* = y_j - \sum_{i=1}^{m} \alpha_i^* y_i K(\mathbf{x}_i, \mathbf{x}_j),\ j \in VS = \{j : \alpha_j^* \neq 0\}$$

Pour le SVM à marge molle, le problème d'optimisation est :

$$\begin{cases} \max_\alpha \{ \sum\limits_{i=1}^{m} \alpha_i - \frac{1}{2} \sum\limits_{i,j=1}^{m} \alpha_i \alpha_j y_i y_j K(\mathbf{x}_i, \mathbf{x}_j) \} \\ \forall i\ 0 \leq \alpha_i \leq C,\ i = 1, ..., m \\ \sum\limits_{i=1}^{m} \alpha_i y_i = 0 \end{cases} \tag{2.46}$$

Avec comme hyperplan optimal :

$$h(\mathbf{x}) = \sum_{i=1}^{m} \alpha_i^* y_i K(\mathbf{x}, \mathbf{x}_i) + w_0^*$$
$$avec\ w_0^* = y_j - \sum_{i=1}^{m} \alpha_i^* y_i K(\mathbf{x}_i, \mathbf{x}_j),\ j \in \{j : 0 < \alpha_j^* < C\}$$

Les fonctions noyau les plus populaires sont les fonctions linéaires $K(\mathbf{x}, \mathbf{y}) = \langle \mathbf{x}, \mathbf{y} \rangle$, les fonctions polynomiales $K(\mathbf{x}, \mathbf{y}) = (\langle \mathbf{x}, \mathbf{y} \rangle + 1)^p$, les fonctions à base radiale (RBF) avec $K(\mathbf{x}, \mathbf{y}) = e^{-\frac{\|\mathbf{x}-\mathbf{y}\|^2}{2\sigma^2}}$ et les fonctions sigmoïdes $K(\mathbf{x}, \mathbf{y}) = \tanh(a\langle \mathbf{x}, \mathbf{y} \rangle - b)$.

2.1.5 Classification avec plus de 2 Classes par SVM

Pour ce qui est la généralisation de deux classes à plusieurs classes, l'une des méthodes utilisées est la méthode dite "un-contre-reste" ("one-versus-rest" en Anglais) qui

consiste à faire pour K classes, K SVM binaires (un pour chaque classe), le i-ème SVM construisant un hyperplan optimal entre la classe i et les K-1 classes restantes. L'autre méthode est "un-contre-un" ("one-versus-one" en Anglais), qui fait $\frac{K(K-1)}{2}$ hyperplans soit un pour chaque couple de classes [5–7]. D'autres méthodes existent aussi comme la séparation des K classes en une seule optimisation proposée dans [7] ou celle appelée DAG SVM (Directed Acyclic Graph SVM) dans [6].

Le SVM et les réseaux de neurones sont de meilleurs outils de classification quand les attributs sont multidimensionnels et continus [8]. Les SVM sont caractérisés par l'utilisation des fonctions de noyau ("kernel functions"), l'absence de minima locaux et les solutions "sparse" grâce aux vecteurs de supports [2]. De plus, le SVM est bien adapté pour les modèles d'apprentissage où le nombre d'attributs est grand par rapport au nombre d'exemples d'entraînement [8], ce qui est le cas pour ce travail de recherche.

2.2 Classificateurs de Bayes Naïf

Ce sont des classificateurs de modèle génératif basés sur l'hypothèse selon laquelle les attributs des entrées sont conditionnellement indépendants sachant la classe [9].

Ce modèle est dit "naïf" car il est extrêmement rare que cette hypothèse soit réalisée. Les classificateurs de modèle génératif cherchent les probabilités a priori $p(C_k)$ pour chaque classe $C_k \in \{C_1, C_2, ..., C_K\}$, puis apprennent un modèle probabiliste $p(\mathbf{x}|C_k)$ pour chaque classe C_k individuellement avec $\mathbf{x} = (x_1, x_2, ..., x_d)$, d étant la dimension des attributs. De cet apprentissage, on obtient les paramètres de la distribution de probabilité choisie pour $p(\mathbf{x}|C_k)$. Les classificateurs de modèle génératif utilisent ensuite le théorème de Bayes pour la classification :

$$p(C_k|\mathbf{x}) = \frac{p(\mathbf{x}|C_k)p(C_k)}{p(\mathbf{x})}$$
$$\Leftrightarrow p(C_k|x_1, x_2, ..., x_d) = \frac{p(x_1, x_2, ..., x_d|C_k)p(C_k)}{p(x_1, x_2, ..., x_d)}$$

Or, grâce à l'hypothèse de l'indépendance conditionnelle des attributs sachant la classe (Bayes naïf) :

$$p(x_1,x_2,...,x_d|C_k) = p(x_1|C_k)p(x_2|C_k)...p(x_d|C_k)$$
$$\Rightarrow p(C_k|x_1,x_2,...,x_d) = \frac{p(x_1|C_k)p(x_2|C_k)...p(x_d|C_k)p(C_k)}{p(x_1,x_2,...,x_d)}$$
$$\Leftrightarrow p(C_k|x_1,x_2,...,x_d) = \frac{p(C_k)\prod_{i=1}^{d} p(x_i|C_k)}{p(x_1,x_2,...,x_d)}$$

p($x_1,x_2,...,x_d$) ne dépend pas de C_k et les valeurs de $x_1,x_2,...,x_d$ étant connu, p($x_1,x_2,...,x_d$) est alors une constante

$\Rightarrow p(C_k|x_1,x_2,...,x_d) \propto p(C_k)\prod_{i=1}^{d} p(x_i|C_k)$

Soit $\tilde{\mathbf{x}}$= ($\tilde{x}_1,\tilde{x}_2,...,\tilde{x}_d$) une nouvelle entrée pour laquelle on veut faire une classification. Sa classe $\tilde{y}$ est alors

$\Rightarrow \tilde{y} \leftarrow \underset{C_k}{\text{argmax}}\ p(C_k)\prod_{i=1}^{d} p(\tilde{x}_i|C_k)$

2.2.1 Modèle Gaussien de Bayes Naïf

Le modèle gaussien naïf de Bayes est utilisé pour des entrées réelles. Par exemple pour un classificateur gaussien naïf de Bayes en dimension d, nous avons :

$$\mathcal{N}(\mathbf{x}|\mu,\Sigma) \stackrel{\Delta}{=} \frac{1}{(2\pi)^{\frac{d}{2}}|\Sigma|^{\frac{1}{2}}} \exp\left(-\frac{1}{2}(\mathbf{x}-\mu)^T\Sigma^{-1}(\mathbf{x}-\mu)\right)$$
$$\Rightarrow p(\mathbf{x}|C_k) = \frac{1}{(2\pi)^{\frac{d}{2}}|\Sigma_k|^{\frac{1}{2}}} \exp\left(-\frac{1}{2}(\mathbf{x}-\mu_k)^T\Sigma_k^{-1}(\mathbf{x}-\mu_k)\right)$$

Les attributs étant conditionnellement indépendants sachant la classe C_k : $\Sigma_{kij} = Cov(x_i,x_j) = 0$

pour $i \neq j$ et $\Sigma_{kii} = Cov(x_i, x_i) = \sigma_{ki}^2$.

$$
\begin{aligned}
& p(\mathbf{x}|C_k) = p(x_1, x_2, ..., x_d|C_k) \\
& \Rightarrow p(\mathbf{x}|C_k) = p(x_1|C_k)p(x_2|C_k)...p(x_d|C_k) \\
& \Rightarrow p(\mathbf{x}|C_k) = \prod_{i=1}^{d} p(x_i|C_k) \\
& \Rightarrow p(\mathbf{x}|C_k) = \frac{1}{(2\pi)^{\frac{d}{2}} \prod_{i=1}^{d} |\sigma_{ki}|} \exp\left(-\sum_{i=1}^{d} \frac{(x_i - \mu_{ki})^2}{2\sigma_{ki}^2} \right)
\end{aligned}
$$

Donc pour un classificateur gaussien naïf de Bayes, la classification de la nouvelle entrée $(\tilde{\mathbf{x}}, \tilde{y})$ est :

$$\Rightarrow \tilde{y} \leftarrow \underset{k}{\text{argmax}}\ \pi_k \prod_{i=1}^{d} \mathscr{N}(\tilde{\mathbf{x}}|\hat{\mu}_{ki}, \hat{\sigma}_{ki}^2)$$

π_k étant la probabilité a priori de la classe C_k.
En effet, soit $\mathscr{D} = \{(\mathbf{x}_1, y_1), (\mathbf{x}_2, y_2), ..., (\mathbf{x}_N, y_N)\}$, l'ensemble d'entraînement, avec $y_i \in \{C_1, C_2, ..., C_K\}$:

$p(\mathbf{x}_n, C_k) = p(C_k)p(\mathbf{x}_n|C_k)$
La fonction de vraissemblance est alors :

$$p(\mathbf{T}, \mathbf{X}|\pi_k, \mu_{ki}, \sigma_{ki^2}) = \prod_{n=1}^{N} \prod_{k=1}^{K} \left(\pi_k \prod_{i=1}^{d} \mathscr{N}(x_{ni}|\mu_{ki}, \sigma_{ki}^2) \right)^{t_{nk}}$$

avec $t_{nk} = \begin{cases} 1 & \text{si } y_n = C_k \\ 0 & \text{sinon.} \end{cases}$, $T_{nk} = t_{nk}, X_{ni} = x_{ni}$ et $\sum_{k=1}^{K} \pi_k = 1$

Pour le modèle gaussien de Bayes naïf, la fonction de vraissemblance est :

$$p(\mathbf{T},\mathbf{X}|\pi_k,\mu_{ki},\sigma_{ki}^2) = \prod_{n=1}^{N}\prod_{k=1}^{K}\left(\pi_k \frac{1}{(2\pi)^{\frac{d}{2}}\prod_{i=1}^{d}|\sigma_{ki}|}\exp\left(-\sum_{i=1}^{d}\frac{(x_{ni}-\mu_{ki})^2}{2\sigma_{ki}^2}\right)\right)^{t_{nk}}$$

Sa log-vraissemblance est :

$$\log(p(\mathbf{T},\mathbf{X}|\pi_k,\mu_{ki},\sigma_{ki}^2)) =$$
$$\sum_{n=1}^{N}\sum_{k=1}^{K} t_{nk}\log(\pi_k) + \sum_{n=1}^{N}\sum_{k=1}^{K} t_{nk}\log\left(\frac{1}{(2\pi)^{\frac{d}{2}}\prod_{i=1}^{d}|\sigma_{ki}|}\exp\left(-\sum_{i=1}^{d}\frac{(x_{ni}-\mu_{ki})^2}{2\sigma_{ki}^2}\right)\right)$$

Nous allons optimiser cette log-vraissemblance sous la condition $\sum_{k=1}^{K}\pi_k = 1$ grâce au lagrangien $\mathrm{L}(\pi_k,\mu_{ki},\sigma_{ki}^2)$:

$$\begin{aligned} L(\pi_k,\mu_{ki},\sigma_{ki}^2) &= \sum_{n=1}^{N}\sum_{k=1}^{K} t_{nk}\log(\pi_k) + \sum_{n=1}^{N}\sum_{k=1}^{K} t_{nk}\log\left(\frac{1}{(2\pi)^{\frac{d}{2}}\prod_{i=1}^{d}|\sigma_{ki}|}\exp\left(-\sum_{i=1}^{d}\frac{(x_{ni}-\mu_{ki})^2}{2\sigma_{ki}^2}\right)\right) \\ &+ \alpha\left(\sum_{k=1}^{K}(\pi_k - 1)\right) \end{aligned} \tag{2.47}$$

α étant un multiplicateur de Lagrange.

$$\Rightarrow L(\pi_k,\mu_{ki},\sigma_{ki}^2) = L_1(\pi_k) + L_2(\mu_{ki},\sigma_{ki}^2) \tag{2.48}$$

Avec :

$$L_1(\pi_k) = \sum_{n=1}^{N}\sum_{k=1}^{K} t_{nk}\log(\pi_k) + \alpha\left(\sum_{k=1}^{K}(\pi_k - 1)\right) \tag{2.49}$$

$$L_2(\mu_{ki}, \sigma_{ki}^2) = \sum_{n=1}^{N}\sum_{k=1}^{K} t_{nk} \log\left(\frac{1}{(2\pi)^{\frac{d}{2}}\prod_{i=1}^{d}|\sigma_{ki}|}\exp\left(-\sum_{i=1}^{d}\frac{(x_{ni}-\mu_{ki})^2}{2\sigma_{ki}^2}\right)\right) \tag{2.50}$$

La solution correspond au point où les dérivées par rapport à π_k, μ_{ki} et σ_{ki}^2 s'annulent. L'équation 2.48 nous donne :

$$\frac{\partial L(\pi_k, \mu_{ki}, \sigma_{ki}^2)}{\partial \pi_k} = \frac{\partial L_1(\pi_k)}{\partial \pi_k} \tag{2.51}$$

$$\frac{\partial L(\pi_k, \mu_{ki}, \sigma_{ki}^2)}{\partial \mu_{ki}} = \frac{\partial L_2(\mu_{ki}, \sigma_{ki}^2)}{\partial \mu_{ki}} \tag{2.52}$$

$$\frac{\partial L(\pi_k, \mu_{ki}, \sigma_{ki}^2)}{\partial \sigma_{ki}^2} = \frac{\partial L_2(\mu_{ki}, \sigma_{ki}^2)}{\partial \sigma_{ki}^2} \tag{2.53}$$

À partir des équations 2.51 et 2.49 nous obtenons :

$$\begin{aligned}
&\frac{\partial L_1(\pi_k)}{\partial \pi_k} = 0 \\
&\Rightarrow \frac{\partial\left(\sum_{n=1}^{N}\sum_{k=1}^{K} t_{nk}\log(\pi_k) + \alpha\left(\sum_{k=1}^{K}(\pi_k - 1)\right)\right)}{\partial \pi_k} = 0 \\
&\Rightarrow \sum_{n=1}^{N} t_{nk}\frac{1}{\pi_k} + \alpha = 0
\end{aligned}$$

$$\Rightarrow \pi_k = \frac{\sum_{n=1}^{N} t_{nk}}{-\alpha} \tag{2.54}$$

En remplaçant cette valeur de π_k dans la condition $\sum_{k=1}^{K} \pi_k = 1$ nous obtenons :

$$\begin{aligned}
&\sum_{k=1}^{K} \frac{\sum_{n=1}^{N} t_{nk}}{-\alpha} = 1 \\
&\Rightarrow \frac{1}{-\alpha} \sum_{k=1}^{K} \sum_{n=1}^{N} t_{nk} = 1 \\
&\Rightarrow -\alpha = \sum_{n=1}^{N} \sum_{k=1}^{K} t_{nk}
\end{aligned}$$

En remplaçant la valeur de $-\alpha$ dans l'équation 2.54, nous avons :

$$\Rightarrow \hat{\pi}_k = \frac{\sum_{n=1}^{N} t_{nk}}{\sum_{n=1}^{N} \sum_{k=1}^{K} t_{nk}} \tag{2.55}$$

$$\Rightarrow \hat{\pi}_k = \frac{\sum_{n=1}^{N} t_{nk}}{N} \tag{2.56}$$

À partir des équations 2.50, 2.52 et 2.53, nous obtenons les paramètres μ_{ki} et σ_{ki}^2 comme suit :

$$\begin{aligned}
\log(L_2(\mu_{ki}, \sigma_{ki}^2)) &= \sum_{n=1}^{N} \sum_{k=1}^{K} \log \left(\frac{1}{(2\pi)^{\frac{d}{2}} \prod_{i=1}^{d} |\sigma_{ki}|} \exp \left(- \sum_{i=1}^{d} \frac{(x_{ni} - \mu_{ki})^2}{2\sigma_{ki}^2} \right) \right)^{t_{nk}} \\
&= \sum_{n=1}^{N} \sum_{k=1}^{K} t_{nk} \log \left(\frac{1}{(2\pi)^{\frac{d}{2}} \prod_{i=1}^{d} |\sigma_{ki}|} \exp \left(- \sum_{i=1}^{d} \frac{(x_{ni} - \mu_{ki})^2}{2\sigma_{ki}^2} \right) \right) \\
&= \sum_{n=1}^{N} \sum_{k=1}^{K} t_{nk} \left(- \frac{d}{2} \log(2\pi) - \sum_{i=1}^{d} \log \left((\sigma_{ki}^2)^{\frac{1}{2}} \right) - \sum_{i=1}^{d} \frac{(x_{ni} - \mu_{ki})^2}{2\sigma_{ki}^2} \right)
\end{aligned}$$

En annulant les dérivées, nous obtenons :

$$\begin{cases} \frac{\partial \log(L_2(\mu_{ki},\sigma_{ki}^2))}{\partial \mu_{ki}} = 0 \\ \frac{\partial \log(L_2(\mu_{ki},\sigma_{ki}^2))}{\partial \sigma_{ki}^2} = 0 \end{cases}$$

$$\Rightarrow \begin{cases} \sum_{n=1}^{N} t_{nk}\left(\frac{(x_{ni}-\hat{\mu}_{ki})}{\hat{\sigma}_{ki}^2}\right) = 0 \\ \sum_{n=1}^{N} t_{nk}\left(-\frac{1}{2\hat{\sigma}_{ki}^2} + \frac{(x_{ni}-\hat{\mu}_{ki})^2}{2(\hat{\sigma}_{ki}^2)^2}\right) = 0 \end{cases}$$

$$\Rightarrow \begin{cases} \frac{1}{\hat{\sigma}_{ki}^2}\sum_{n=1}^{N} t_{nk}x_{ni} = \frac{\hat{\mu}_{ki}}{\hat{\sigma}_{ki}^2}\sum_{n=1}^{N} t_{nk} \\ \frac{1}{2(\hat{\sigma}_{ki}^2)^2}\sum_{n=1}^{N} t_{nk}(x_{ni}-\hat{\mu}_{ki})^2 = \frac{1}{2\hat{\sigma}_{ki}^2}\sum_{n=1}^{N} t_{nk} \end{cases}$$

$$\Rightarrow \begin{cases} \hat{\mu}_{ki} = \frac{\sum_{n=1}^{N} t_{nk}x_{ni}}{\sum_{n=1}^{N} t_{nk}} \\ \hat{\sigma}_{ki}^2 = \frac{\sum_{n=1}^{N} t_{nk}(x_{ni}-\hat{\mu}_{ki})^2}{\sum_{n=1}^{N} t_{nk}} \end{cases}$$

Finalement, la classification d'une nouvelle entrée $(\tilde{\mathbf{x}}, \tilde{y})$, pour un classificateur gaussien naïf de Bayes sera :

$$\tilde{y} \leftarrow \underset{k}{\text{argmax}}\ \pi_k \prod_{i=1}^{d} \mathcal{N}(\tilde{\mathbf{x}} | \hat{\mu}_{ki}, \hat{\sigma}_{ki}^2)$$

2.2.2 Modèle Multinoulli de Bayes Naïf

Le modèle multinoulli de Bayes naïf est utilisé pour les entrées discrètes. La distribution multinoulli est une distribution telle que [10] :

$$Cat(x_i|\mu_i) \stackrel{\Delta}{=} \prod_{j=1}^{M} \mu_{ij}^{x_{ij}} \quad \text{avec} \quad x_i \in \{0,1\}^M \quad \text{et} \quad \sum_{j=1}^{M} x_{ij} = 1 \tag{2.57}$$

Par l'hypothèse de Bayes naïf nous avons : $p(\mathbf{x}_n|C_k) = \prod_{i=1}^{d} p(x_{ni}|C_k)$

La fonction de vraissemblance est :

$$p(\mathbf{T}, \mathbf{X}|\pi_k, \mu_{ki}) = \prod_{n=1}^{N}\prod_{k=1}^{K}\left(\pi_k \prod_{i=1}^{d} Cat(x_{ni}|\mu_{ki})\right)^{t_{nk}}$$
$$\Rightarrow p(\mathbf{T}, \mathbf{X}|\pi_k, \mu_{ki}) = \prod_{n=1}^{N}\prod_{k=1}^{K}\left(\pi_k \prod_{i=1}^{d}\prod_{j=1}^{M} \mu_{kij}^{x_{nij}}\right)^{t_{nk}}$$

Avec les contraintes :

$$\sum_{k=1}^{K} \pi_k = 1 \quad \text{et} \quad \sum_{j=1}^{M} \mu_{kij} = 1 \quad \text{car} \quad \mu_{kij} = p(x_i = j|C_k) \tag{2.58}$$

Sa log-vraissemblance est :

$$\log(p(\mathbf{T}, \mathbf{X}|\pi_k, \mu_{kij})) = \sum_{n=1}^{N}\sum_{k=1}^{K} t_{nk} \log(\pi_k) + \sum_{n=1}^{N}\sum_{k=1}^{K}\sum_{i=1}^{d}\sum_{j=1}^{M} t_{nk} x_{nij} \log(\mu_{kij})$$

Nous allons optimiser cette log-vraissemblance sous les contraintes 2.58 grâce au la-

grangien $\mathrm{L}(\pi_k, \mu_{kij})$:

$$\begin{aligned} L(\pi_k, \mu_{kij}) &= \sum_{n=1}^{N}\sum_{k=1}^{K} t_{nk}\log(\pi_k) + \sum_{n=1}^{N}\sum_{k=1}^{K}\sum_{i=1}^{d}\sum_{j=1}^{M} t_{nk}x_{nij}\log(\mu_{kij}) \\ &+ \alpha\left(\sum_{k=1}^{K}\pi_k - 1\right) + \lambda\left(\sum_{j=1}^{M}\mu_{kij} - 1\right) \end{aligned} \tag{2.59}$$

α et λ étant des multiplicateurs de Lagrange.

$$\Rightarrow L(\pi_k, \mu_{kij}) = L_1(\pi_k) + L_2(\mu_{kij}) \tag{2.60}$$

Avec :

$$L_1(\pi_k) = \sum_{n=1}^{N}\sum_{k=1}^{K} t_{nk}\log(\pi_k) + \alpha\left(\sum_{k=1}^{K}\pi_k - 1\right) \tag{2.61}$$

$$L_2(\mu_{kij}) = \sum_{n=1}^{N}\sum_{k=1}^{K}\sum_{i=1}^{d}\sum_{j=1}^{M} t_{nk}x_{nij}\log(\mu_{kij}) + \lambda\left(\sum_{j=1}^{M}\mu_{kij} - 1\right) \tag{2.62}$$

Les paramètres π_k sont obtenus comme pour le modèle gaussien (cf. équation 2.56).

Pour obtenir les paramètres μ_{kij}, nous fixons à zéro les dérivées de L_2 :

$$\begin{aligned} &\frac{\partial\left(\sum_{n=1}^{N}\sum_{k=1}^{K}\sum_{i=1}^{d}\sum_{j=1}^{M} t_{nk}x_{nij}\log(\mu_{kij}) + \lambda\left(\sum_{j=1}^{M}\mu_{kij} - 1\right)\right)}{\partial\mu_{kij}} = 0 \\ &\Rightarrow \sum_{n=1}^{N} t_{nk}x_{nij}\frac{1}{\mu_{kij}} + \lambda = 0 \\ &\Rightarrow \frac{1}{\mu_{kij}}\sum_{n=1}^{N} t_{nk}x_{nij} = -\lambda \end{aligned}$$

$$\Rightarrow \mu_{kij} = \frac{\sum_{n=1}^{N} t_{nk}x_{nij}}{-\lambda} \tag{2.63}$$

Or $\sum_{j=1}^{M} \mu_{kij} = 1$ (cf. les équations 2.58)

$$\Rightarrow \sum_{j=1}^{M} \left(\frac{1}{-\lambda} \sum_{n=1}^{N} t_{nk} x_{nij} \right) = 1$$
$$\Rightarrow \sum_{j=1}^{M} \sum_{n=1}^{N} t_{nk} x_{nij} = -\lambda$$
$$\Rightarrow \sum_{n=1}^{N} t_{nk} \sum_{j=1}^{M} x_{nij} = -\lambda$$

Or $\sum_{j=1}^{M} x_{nij} = 1$ (cf. l'équation 2.57)

$$\Rightarrow -\lambda = \sum_{n=1}^{N} t_{nk}$$

En remplaçant $-\lambda$ dans l'équation 2.63, nous obtenons les paramètres recherchés pour classer une nouvelle entrée :

$$\Rightarrow \hat{\mu}_{kij} = \frac{\sum_{n=1}^{N} t_{nk} x_{nij}}{\sum_{n=1}^{N} t_{nk}} \tag{2.64}$$

On choisit la distribution de $p(\mathbf{x}_i|C_k)$ en fonction des données d'apprentissage. Et selon la distribution de $p(\mathbf{x}_i|C_k)$, on aura un classificateur de Bayes naïf gaussien si $p(\mathbf{x}_i|C_k)$ est une distribution normale(gaussienne), multinoulli (si $p(\mathbf{x}_i|C_k)$ est une distribution multinoulli) ou Bernoulli (si $p(\mathbf{x}_i|C_k)$ est une distribution de Bernoulli).

Les classifieurs Bayes naïf sont comparables aux classificateurs qui ont de meilleures performances bien que leur hypothèse d'indépendance des attributs sachant la classe soit généralement non réaliste pour les données de la vie courante [11–13].

2.3 k Plus Proches Voisins, k-PPV(k-NN)

Pour cette technique de classification, une observation non classée prend l'étiquette de la classe majoritaire dans les k exemples d'apprentissage les plus proches selon une fonction de distance choisie. Les plus importantes fonctions de distance utilisées sont [8] :

- Minkowski : $d(\mathbf{x},\mathbf{y}) = (\sum_{i=1}^{m} |x_i - y_i|^r)^{\frac{1}{r}}$
- Manhattan : $d(\mathbf{x},\mathbf{y}) = \sum_{i=1}^{m} |x_i - y_i|$
- Chebychev : $d(\mathbf{x},\mathbf{y}) = \max_{i=1}^{m} |x_i - y_i|$
- Euclidienne : $d(\mathbf{x},\mathbf{y}) = (\sum_{i=1}^{m} |x_i - y_i|^2)^{\frac{1}{2}}$
- Camberra : $d(\mathbf{x},\mathbf{y}) = \sum_{i=1}^{m} \frac{|x_i - y_i|}{|x_i + y_i|}$
- Corrélation de rang de Kendall :
  $d(\mathbf{x},\mathbf{y}) = 1 - \frac{2}{m(m-1)} \sum_{i=j}^{m} \sum_{j=1}^{i-1} \text{sign}(x_i - x_j)\text{sign}(y_i - y_j)$

Toutefois, parmi ces distances, la plus souvent utilisée est la distance euclidienne. Notons aussi qu'il existe plusieurs variantes de k-PPV(k-NN). Un exemple parmi ces dernières est le cas où au lieu de considérer une seule voix pour chaque plus proche voisin, chaque voix est plutôt pondérée en fonction de la distance au point qu'on cherche à classer [3]. La puissance de k-PPV a été prouvée dans plusieurs domaines même si cette méthode de classification possède quelques défauts tels que le stockage de beaucoup de données (car elle exige le stockage des données d'apprentissage), la sensibilité au choix de la fonction de distance et la difficulté de choisir un k adéquat [8].

2.4 Régression Logistique

La régression logistique est un modèle d'apprentissage qui, pour un ensemble d'entraînement $\mathscr{D} = \{(\mathbf{x}_1, y_1), (\mathbf{x}_2, y_2), ..., (\mathbf{x}_N, y_N)\}$ avec $y_i \in \{C_1, C_2, ..., C_K\}$, apprend direc-

tement p($C_k|\mathbf{x}_n$) sans passer par l'apprentissage de p($\mathbf{x}_n|C_k$) :

$$p(C_k|\mathbf{x}_n) = \frac{\exp(\mathbf{w}_k^T \mathbf{x}_n)}{\sum_{j=1}^{K} \exp(\mathbf{w}_j^T \mathbf{x}_n)} \tag{2.65}$$

La fonction de vraissemblance est alors :

$$\begin{aligned} p(\mathbf{T}, \mathscr{D}|\mathbf{W}) &= \prod_{n=1}^{N} p(y_n|\mathbf{x}_n) \\ &= \prod_{n=1}^{N}\prod_{k=1}^{K} p(C_k|\mathbf{x}_n)^{t_{nk}} \end{aligned}$$

$\mathbf{T}$ étant une matrice $N \times K$ avec comme éléments $t_{nk} = 1$ si $y_n = C_k$ et $t_{nk} = 0$ sinon.
Nous calculons la fonction de coût $E(\mathscr{D}; \mathbf{W})$ en utilisant la log-vraissemblance négative

$$\begin{aligned} E(\mathscr{D}; \mathbf{W}) &= -\log\Big(p(\mathbf{T}, \mathscr{D}|\mathbf{W})\Big) \\ &= -\sum_{n=1}^{N}\sum_{k=1}^{K} t_{nk} \log\Big(p(C_k|\mathbf{x}_n)\Big) \\ &= -\sum_{n=1}^{N}\sum_{k=1}^{K} t_{nk} \log\left(\frac{exp(\mathbf{w}_k^T \mathbf{x}_n)}{\sum_{j=1}^{K} \exp(\mathbf{w}_j^T \mathbf{x}_n)}\right) \\ &= -\sum_{n=1}^{N}\sum_{k=1}^{K} t_{nk}\left(\mathbf{w}_k^T \mathbf{x}_n - \log\left(\sum_{j=1}^{K} \exp(\mathbf{w}_j^T \mathbf{x}_n)\right)\right) \end{aligned}$$

$$\Rightarrow E(\mathscr{D}; \mathbf{W}) = -\sum_{n=1}^{N}\sum_{k=1}^{K} t_{nk}\left(\mathbf{w}_k^T \mathbf{x}_n - \log\left(\sum_{j=1}^{K} \exp(\mathbf{w}_j^T \mathbf{x}_n)\right)\right) \tag{2.66}$$

Le gradient de la fonction de coût (2.66)est alors :

$$\nabla_{\mathbf{w}_k} E(\mathscr{D}; \mathbf{W}) = -\sum_{n=1}^{N} t_{nk}\left(\mathbf{x}_n - \left(\frac{\exp(\mathbf{w}_k^T \mathbf{x}_n)}{\sum_{j=1}^{K} \exp(\mathbf{w}_j^T \mathbf{x}_n)}\right)\mathbf{x}_n\right)$$

$$\Rightarrow \nabla_{\mathbf{w}_k} E(\mathscr{D}; \mathbf{W}) = \sum_{n=1}^{N} \Big(p(C_k|\mathbf{x}_n) - t_{nk} \Big) \mathbf{x}_n \tag{2.67}$$

Comme nous n'avons pas de solution de forme fermée, pour trouver la solution de l'optimisation de $E(\mathbf{W})$, on recourt aux méthodes basées sur le gradient(méthode du gradient descendant, la méthode de Newton-Raphson, etc.).

2.5 Gradient Stochastique Descendant

La méthode du gradient stochastique descendant (stochastic gradient descent SGD) est une des méthode d'optimisation basée sur le gradient. Soit un ensemble d'entraînement $\mathscr{D} = \{\mathbf{z}_1, \mathbf{z}_2, ..., \mathbf{z}_N\}$ avec $\mathbf{z}_i = (\mathbf{x}_i, y_i)$ et $E(\mathbf{z_i}, \mathbf{w})$ une fonction de coût qu'on veut optimiser. La solution de l'optimisation par le gradient descendant est obtenue par des itérations successives de la forme [14] :

$$\mathbf{w}_{t+1} = \mathbf{w}_t - \eta \frac{1}{N} \sum_{n=1}^{N} \nabla_{\mathbf{w}} E(\mathbf{z}_n, \mathbf{w}) \tag{2.68}$$

η est appelé le taux d'apprentissage et $\frac{1}{N} \sum_{n=1}^{N} E(\mathbf{z}_n, \mathbf{w})$ est le risque empirique. Pour le gradient stochastique descendant, au lieu de calculer le gradient du risque empirique, on le remplace par son estimation obtenue grâce à un seul exemple d'entraînement $\mathbf{z}_t$ choisi de façon aléatoire à chaque itération :

$$\mathbf{w}_{t+1} = \mathbf{w}_t - \eta \nabla_{\mathbf{w}} E(\mathbf{z}_t, \mathbf{w}) \tag{2.69}$$

Le gradient stochastique descendant peut être utilisé par plusieurs classificateurs en fonction du choix de sa fonction de coût (la régression logistique (LR), les machines de vecteurs de support (SVM), la régression de Ridge, etc.).

2.6 Validation Croisée (K-Fold Cross-Validation)

La validation croisée consiste à diviser les données d'apprentissage en K sous échantillons de même taille. L'apprentissage est alors fait sur K-1 échantillons et le test sur

l'échantillon qui reste. On retient ensuite le taux de réussite (taux d'erreur) pour cet échantillon de test. Soit T_i, le taux de réussite de l'échantillon i. On refait le processus en faisant passer chacun des K échantillons dans le rôle de test. À la fin, on fait la moyenne des taux de réussite trouvés pour chaque échantillon [3], soit

$$T_{moy} = \frac{1}{K} \sum_{i=1}^{K} T_i \tag{2.70}$$

Comme nous avons une faible quantité de données (51 vidéos), nous avons aussi utilisé la technique dite "leave-one-out cross-validation". Celle-ci est une variante de "K-fold cross-validation" avec K qui est la taille de l'ensemble de données utilisées. On teste alors sur un seul exemple, les autres éléments étant des exemples d'apprentissage. Les autres étapes sont les mêmes que pour le "K-fold cross-validation".

BIBLIOGRAPHIE

[1] Bernhard E Boser, Isabelle M Guyon, and Vladimir N Vapnik. A training algorithm for optimal margin classifiers. In *Proceedings of the fifth annual workshop on Computational learning theory*, pages 144–152. ACM, 1992.

[2] Nello Cristianini and John Shawe-Taylor. *An introduction to support vector machines and other kernel-based learning methods*. Cambridge university press, 2000.

[3] Antoine Cornuéjols and Laurent Miclet. *Apprentissage artificiel : concepts et algorithmes*. Editions Eyrolles, 2011.

[4] Ingo Steinwart and Andreas Christmann. *Support vector machines*. Springer Science & Business Media, 2008.

[5] Vladimir Naumovich Vapnik and Vlamimir Vapnik. *Statistical learning theory*, volume 1. Wiley New York, 1998.

[6] John C Platt, Nello Cristianini, and John Shawe-Taylor. Large margin dags for multiclass classification. In *nips*, volume 12, pages 547–553, 1999.

[7] Jason Weston and Chris Watkins. Support vector machines for multi-class pattern recognition. In *ESANN*, volume 99, pages 219–224, 1999.

[8] Sotiris B Kotsiantis, I Zaharakis, and P Pintelas. Supervised machine learning : A review of classification techniques, 2007.

[9] Christopher M Bishop. *Pattern Recognition and Machine Learning (Information Science and Statistics)*. Springer, 2006.

[10] Kevin P Murphy. *Machine learning : a probabilistic perspective*. MIT press, 2012.

[11] Pedro Domingos and Michael Pazzani. On the optimality of the simple bayesian classifier under zero-one loss. *Machine learning*, 29 :103–130, 1997.

[12] Andrew McCallum, Kamal Nigam, et al. A comparison of event models for naive bayes text classification. In *AAAI-98 workshop on learning for text categorization*, volume 752, pages 41–48. Citeseer, 1998.

[13] Richard O Duda, Peter E Hart, and David G Stork. *Pattern classification*. John Wiley & Sons, 2001.

[14] Léon Bottou. Stochastic gradient descent tricks. In *Neural Networks : Tricks of the Trade*, pages 421–436. Springer, 2012.

CHAPITRE 3

HIGH-FREQUENCY SPECTRAL ENERGY MAP ESTIMATION BASED GAIT ANALYSIS SYSTEM USING A DEPTH CAMERA FOR PATHOLOGY DETECTION

Dans ce chapitre, nous exposons notre article accepté pour la conférence "International Conference on Image Analysis and Recognition" : ICIAR 2016 se déroulant du 13 au 15/07/2016 à Póvoa de Varzim, Portugal. Nous le présentons dans sa langue originale de soumission.

High-Frequency Spectral Energy Map Estimation Based Gait Analysis System Using a Depth Camera for Pathology Detection

Didier Ndayikengurukiye and Max Mignotte
Département d'Informatique et de Recherche Opérationnelle (DIRO),Université de Montréal, Québec, Canada

abstract

This paper presents a new and simple gait analysis system, from a depth camera placed in front of a subject walking on a treadmill, capable of detecting a healthy gait from an impaired one. Our system relies on the fact that a normal or healthy walk typically exhibits a smooth motion (depth) signal, at each pixel with less high-frequency spectral energy content than an impaired or abnormal walk. Thus, the estimation of a map showing the location and the amplitude of the high-frequency spectral energy (HFSE), for each subject, allows clinicians to visually quantify and localize the different impaired body parts of the patient and to quickly detect a possible disease. Even if the HFSE maps obtained are clearly intuitive for a rapid clinical diagnosis, the proposed system makes

an automatic classification between normal gaits and those who are not with success rates ranging from 88.23% to 92.15%.

3.1 Introduction

The human gait movement is an essential and complex process of the human activity and also a remarkable example of collaborative interactions between the neurological, articular and musculoskeletal systems working effectively together. When everything is working properly, the healthy locomotor system produces a stable gait and a highly consistent, symmetric (nice) walking pattern [1, 2].

This is why human gait impairment is often an important (and sometimes the first) clinical manifestation and indication of various medical disorders. In fact, abnormal or atypical gait can be caused by different factors, either orthopedic (hip injuries, bone malformations, etc.), muscular (weakness, dystrophy, fiber degeneration, etc.), neurological (Parkinson's disease, stroke [3], spinal stenosis, etc.) or neuropsychiatric (autism, schizophrenia, etc.). As a consequence, gait analysis is important (because possibly highly informative) and increasingly used nowadays for the diagnosis of many different types (and degrees) of diseases. In addition, it also exploited as a reliable and accurate indicator for early detection (and follow-up) of a wide range of pathologies.

In this field, the value of sophisticated, marker-based, video-based gait analysis is well established and have also proved their efficiency. Nevertheless, in order to be used, as an early (and fast) diagnostic tool, it is now important to design a reliable and accurate imaging system that is also inexpensive, non-invasive, fast, easy to set up and suitable for small room and daily clinical [4–6] (or home [7]) usage. This has now become possible thanks to the recent technological progress in depth sensor technology. In this paper, we focus on this kind of approach and introduce a new gait analysis system with the above mentioned advantages and characteristics over more sophisticated approaches. This new gait analysis system aims at distinguishing the healthy (human) gait from the impaired ones. In addition, our system localizes the affected body side of the patient and quantify the patients' gait pattern abnormality or alterations of a human subject. We hope this

approach will be exploited, for example, as a good indicator or as a first interesting screening for a possible (orthopedic, muscular or neurological) disease, prior to a more thorough examination by a specialist doctor.

3.2 Previous Work

Current gait analysis systems can be performed with or without markers. Among the marker-based, gait analysis approaches, we can mention the sophisticated Vicon motion-tracking and capture system [8] which offers millimeter resolution of 3D spatial displacements. On one hand, this system is very accurate. On the other hand, the high cost of this system (which consists in real-time tracking multiple infrared red (IR) reflective markers with multiple IR cameras [9]), inhibits its widespread usage for routine clinical practices (since it requires lots of space, time, and expertise to be installed and used).

Therefore, marker-less systems are a promising alternative for clinical environments and are often regarded as easy-to-set-up, easy-to-use, and non-invasive. They are either based on stereo-vision [10], structured light [11], or time-of-flight (TOF) [12] technologies. Although low-cost, the setup and calibration procedure of these systems remain complex. Besides, stereo vision-based systems [13] are not guaranteed to work well if the patient's outfit lacks texture.

An interesting alternative is to use the recent Kinect^{TM} sensor which is based on structured light combined with machine learning technology and two other computer vision techniques ; depth from focus and depth from stereo. The Kinect^{TM} is robust to texture-less surfaces, accurate and remains also compact and very affordable. This new sensor is able to real-time provide an image sequence where the value of each pixel is proportional to the inverse of the depth at each pixel location with a good accuracy. As interesting feature, the Kinect^{TM} camera is also capable to offer (*via* a machine learning subsystem) a real-time estimation of a set (of 20) 3D points representing the different joints of the human body (by selecting the skeleton *mode* of this sensor). This rough skeleton model was exploited by some authors [7, 14] in order to measure spatial-temporal gait variability (such as the stride duration, speed, etc.) and are compared to those ob-

tained with the high-end Vicon MX system. They found that the Kinect was capable of providing accurate and robust results for some gait parameters, but further research is under way to see if these parameters can be subsequently used for a reliable gait analysis and classification system.

Amongst the existing gait analysis system which are based on a direct analysis of a depth map (related to a human walking session on a treadmill), and recorded by a Kinect^{TM}, as the system proposed in this work (see Fig. 3.1), we can cite the feasibility study proposed in [5] and tested on 6 subjects. In this work, the authors simply computed the mean of the obtained depth image sequence (over a gait cycle or a longer period) in order to compress the gait image sequence into a single image which was finally called a depth energy image (DEI). Through this DEI image, the authors were able to distinguish both visually and quantitatively (through the measurement of asymmetry indexes) an abnormal gait and more precisely possible asymmetries in the gait pattern (a symmetric walk generating a DEI exhibiting a symmetric silhouette, in terms of mean depth and conversely). In the same spirit, the authors in [6] propose to quantify the possible asymmetries between the two depth signals of the legs by first dividing each gait cycle in two sub-cycles (left and right steps), and by comparing these two sub-cycles, in terms of depth difference, after a rough spatial and temporal registration procedure. In fact, the two above-mentioned studies use (with many other studies) the notion of possible asymmetry between the depth signals of the legs or, more precisely, the amplitude difference between the right and left legs obtained by the two phases of the gait cycle, as main and relevant measure, for an abnormal or impaired human gait.

Nevertheless, this asymmetry measure should rather be computed, not directly on the pixel-wise depth signals (recorded by the depth sensor) but rather on some interesting features of this depth signal. In the case of an abnormal or impaired human gait, the depth signal exhibits, in time (and for some pixels, often located at the lower limbs), a continuous but (possibly locally) rugged, unsmooth depth signal or function describing in fact, an irregular leg motion (chaotic, unstable with possible sharp transitions with even singularities in time like shock waves or discontinuities eventually sometimes caused by pain due to physical damage or without pain caused by neurological damage. In this

case, the unsmooth behavior of the depth signal comprises some high-frequency harmonics that we can detect and eventually on which we can then compute some asymmetry indexes.

More precisely, in our application we have decided to quantify the atypical gait by exploiting asymmetry measures computed on a map exhibiting the high-frequency spectral (energy) content of the depth signal of each pixel as interesting and spectral more informative feature of the raw depth signal.

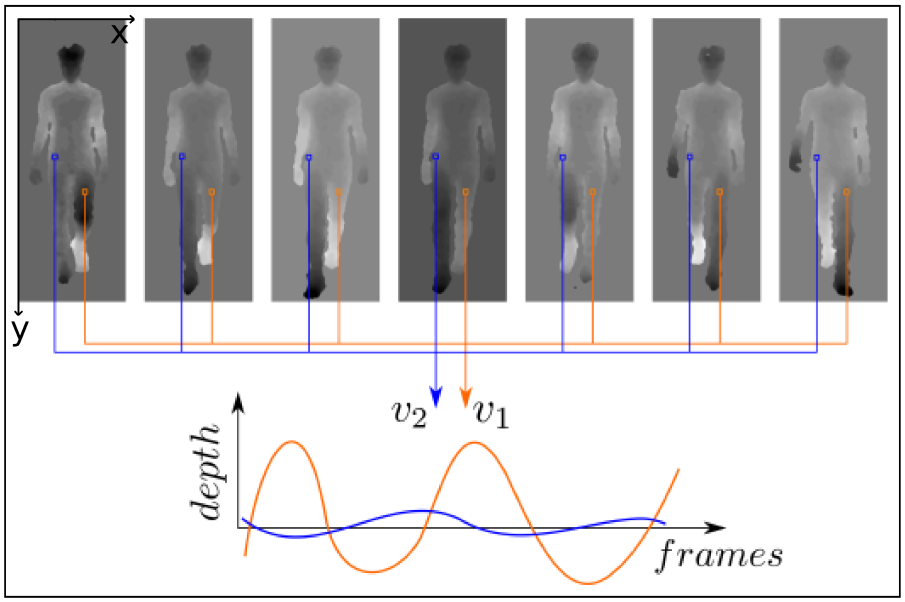

FIGURE 3.1: Example of two depth signals for a gait cycle of a human subject : pixel on the hip (blue curve) and pixel on the thigh (orange curve).

3.3 Data Description and Pre-Processing

For the experiments, 17 (healthy) subjects (young male adults, 26.7 ± 3.8 years old, 179.1 ± 11.5 cm height and 75.5 ± 13.6 kg with no reported gait issues) were asked to walk normally on a treadmill (Life Fitness F3) with or without simulated length leg discrepancy (LLD). Every subject had to walk normally (group A), then with a 5 *cm* sole, impairing the normal walk, under the left foot (group B), then with the sole under the

right foot (group C). After a habituation period of about 2 min, their normal speed was determined and their gait movement was simultaneously recorded using an inexpensive commercial Kinect^{TM} depth camera placed in front of the subject. The Kinect sensor outputs 30 depth maps per second (30 fps), with a resolution of 640 per 480 pixels and for all sequences, the same relative position and distance between the treadmill and the sensor were kept constant in order for the human subject to be located within the same image area. Therefore, the dataset contains 51 different video sequences of a human walk (of approximately 5 minutes long and containing around 180 gait cycles) with or without a simulated length leg discrepancy (LLD) issue which will be analyzed by our automatic gait analysis system. The institutional ethics review board approved the study.

Since the scene took place in a non-cluttered room where the treadmill is in the same position relatively to the camera, a silhouette extraction strategy (background and treadmill removal) can be easily defined as proposed in [15]. Finally, each sequence is filtered with $(3 \times 3 \times 3)$ median filter to reduce the noise level, while preserving the important image (sequence) features, i.e., spatial or depth discontinuities (see Fig. 3.2).

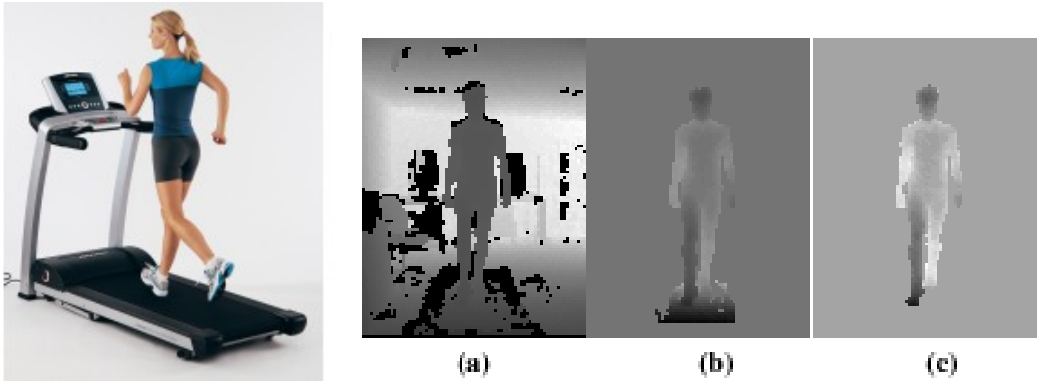

FIGURE 3.2: Setup and pre-processing steps : (a) Original depth map, (b) After the background removal, (c) After the treadmill removal and contrast adjustment.

3.4 Proposed Model

Our model is based on the idea that, for a normal gait, the depth signal of each pixel of a human subject is smooth with little discontinuity. Conversely for a pathological gait

(*i.e.*, associated to a possible pathology), the (pixel-wise) depth signal is not so smooth and exhibits some discontinuities which are in fact expressed by a greater amplitude of its high-frequency spectral energy.

Formally, let $s_p(t)$ be the depth signal of the pixel p. We compute the energy of the Fourier Transform of each pixel's depth signal to obtain $|S_p(\nu)|^2$. This energy spectrum is then high-pass filtered (by setting to zero all the energy values associated with frequencies that are less than a threshold τ, $\tau = 8$ *unities*[1] obtained by trial and error in our case) to estimate the high-frequency spectral energy (HFSE) content at each location of the gait movement. To highlight some relevant features on this HFSE map, this one is then thresholded (by setting to zero all energy value below $\rho = 85$) [2] to better localize the areas with a HFSE content (in terms of size, shape and difference between the left and right legs). In the case of a pathological gait, the unsmooth behavior of a depth signal comprises some high-frequency harmonics showing areas of high energy values that we can easily detect especially when this map is shown in pseudo colors (see Fig. 3.3). In addition, this allows the clinician to visually quantify and localize the different impaired body parts of the patient.

In order to now automatically classify a healthy gait from an impaired one, we extract three relevant features on this map at the lower limb level (between $\frac{1}{2}H$ and $\frac{1}{4}H$ with H the image height). These features are mainly based on the difference of the HFSE content between the left and right legs since visually, we can differentiate a healthy gait from an impaired one from the asymmetry between these two areas. To this end, we first calculate the axis of symmetry of the map (see the algorithm in Appendix) and let L and R be respectively the area occupied by the pixels whose energy values are non-zero and are located to the left (and right) of the axis of symmetry of the image of HFSE. The first considered feature is $\frac{L}{L+R}$, the second feature is $\frac{R}{L+R}$ and the third is $2 \times \frac{L}{R}$. We have normalized the first two features because the silhouettes of the subjects are usually not the same size. In addition, we have doubled the ratio to strengthen small differences

[1] τ : 1 $unity = 0.0586Hz$ thus $\tau \approx 0.47Hz$

[2] ρ has no unity because the value of energy is transformed in greyscale (value between 0 and 255)

between some ratio. These three features are used to train and test the Gaussian Naive Bayes (GNB), the k-Nearest Neighbors (k-NN), the Logistic Regression (LR) and the Support Vector Machine (SVM) classifiers.

3.5 Experimental Results

We performed experimentations on all 17 subjects and obtained 3 HFSE maps for each one. We treated these maps as it is shown by Fig. 3.3 for subject S15. As we can see, the classification of the maps in two categories (pathological or not) or in three categories (without heel, heel under left foot or heel under right foot) is easy for a human operator. Table 3.1 shows the value of the three features computed on the S15 thresholded HFSE map at lower limbs.

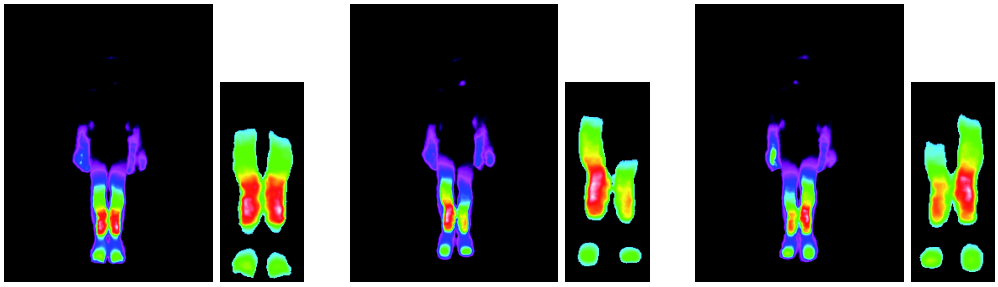

(a) **(b)** **(c)**

FIGURE 3.3: HFSE maps for the S15 subject : (a) Without heel (and thresholded HFSE map at lower limbs) (b) Heel under left foot (and thresholded HFSE map at lower limbs) (c) Heel under right foot (and thresholded HFSE map at lower limbs).

TABLE 3.1: Features for the S15 subject

	normalized left area $\frac{L}{L+R}$	normalized right area $\frac{R}{L+R}$	double ratio $2 \times \frac{L}{R}$
Without heel : A	0.52	0.48	2.16
Heel under left foot : B	0.62	0.38	3.29
Heel under right foot : C	0.42	0.58	1.44

Finally, we did the classification using the Gaussian Naive Bayes (GNB), the k-Nearest Neighbors (k-NN), the Logistic Regression (LR) and Support Vector Machine (SVM) (with linear, polynomial[degree=3], radial basis function[RBF] and sigmoid function as kernel function respectively) classifiers. We use the library from Pedregosa et al. [16] for all the four classifiers. Because we have a relatively small number of maps, we ordered the 51 maps randomly and we take one as a test set and the rest as training set. We repeat the process for all the maps and at the end we average the results (leave one cross-validation). Other experiments are made by dividing the 51 maps into k parts. Each of the k parts is taken as a test set and the k-1 others as training set. We also made the average of the results (k-fold cross-validation). The classification results are shown in Table 3.2 for the logistic regression and SVM models because we kept the classifiers giving the best performance (SVM best kernel : cubic polynomial).

TABLE 3.2: Classification success rate of 51 HFSE maps of 17 subjects in two classes (normal or not) and in three classes (A, B, C) for logistic regression (left) and support vector machine (right) (LOOCV : Leave One Out Cross-Validation, k : k-fold cross-validation)

	2 classes	3 classes
LOOCV	90.20%	88.24%
$k = 5$	86.36%	88.36%
$k = 4$	86.06%	88.46%
$k = 3$	86.28%	88.24%

	2 classes	3 classes
LOOCV	92.16%	88.24%
$k = 5$	88.36%	88.36%
$k = 4$	84.62%	88.46%
$k = 3$	66.67%	88.24%

3.6 Conclusion

In this paper, we have presented a new gait analysis system that is low cost, marker-less, non-invasive, simple to install and requiring a small room. The estimation of a map showing the location and the amplitude of the high-frequency spectral energy, obtained from each subject, allows the clinician to visually quantify and localize the different impaired body parts of the patient. We hope this approach will be exploited, for example, as a good indicator or as a first interesting screening for a possible (orthopedic, muscular or neurological) disease, prior to a more thorough examination by a specialist doctor. The proposed system is also capable to automatically classify between healthy patients and those who are not and to automatically localize the impaired body parts of the patient (right or left) with success rates ranging from 88.23% to 92.15% for SVM and 88.23% to 90.19% for logistic regression on test data.

BIBLIOGRAPHIE

[1] Joel Loizeau, Paul Allard, Morris Duhaime, and Bernard Landjerit. Bilateral gait patterns in subjects fitted with a total hip prosthesis. *Archives of physical medicine and rehabilitation*, 76(6) :552–557, 1995.

[2] J Hamill, BT Bates, and KM Knutzen. Ground reaction force symmetry during walking and running. *Research Quarterly for Exercise and Sport*, 55(3) :289–293, 1984.

[3] Lisa D Alexander, Sandra E Black, Kara K Patterson, Fuqiang Gao, Cynthia J Danells, and William E McIlroy. Association between gait asymmetry and brain lesion location in stroke patients. *Stroke*, 40(2) :537–544, 2009.

[4] Bruce Carse, Barry Meadows, Roy Bowers, and Philip Rowe. Affordable clinical gait analysis : An assessment of the marker tracking accuracy of a new low-cost optical 3d motion analysis system. *Physiotherapy*, 99(4) :347 – 351, 2013.

[5] Caroline Rougier, Edouard Auvinet, Jean Meunier, Max Mignotte, and Jacques A de Guise. Depth energy image for gait symmetry quantification. In *Engineering in Medicine and Biology Society, EMBC, 2011 Annual International Conference of the IEEE*, pages 5136–5139. IEEE, 2011.

[6] E. Auvinet, F. Multon, and J. Meunier. Lower limb movement asymmetry measurement with a depth camera. In *Engineering in Medicine and Biology Society (EMBC), 2012 Annual International Conference of the IEEE*, pages 6793–6796, Aug 2012.

[7] Moshe Gabel, Ran Gilad-Bachrach, Erin Renshaw, and Assaf Schuster. Full body gait analysis with kinect. In *Engineering in Medicine and Biology Society (EMBC), 2012 Annual International Conference of the IEEE*, pages 1964–1967. IEEE, 2012.

[8] Motion capture systems from vicon.

[9] François Potdevin, Christophe Gillet, Franck Barbier, Yann Coello, and Pierre Moretto. The study of asymmetry in able-bodied gait with the concept of propulsion and brake. In *9th Symposium on 3D Analysis of Human Movement, Valenciennes, France*, 2006.

[10] Nalpantidis Lazaros, Georgios Christou Sirakoulis, and Antonios Gasteratos. Review of stereo vision algorithms : from software to hardware. *International Journal of Optomechatronics*, 2(4) :435–462, 2008.

[11] Joaquim Salvi, Jordi Pages, and Joan Batlle. Pattern codification strategies in structured light systems. *Pattern Recognition*, 37(4) :827–849, 2004.

[12] Miles Hansard, Seungkyu Lee, Ouk Choi, and Radu Horaud. *Time-of-flight cameras*. Springer, 2013.

[13] A. Leu, D. Ristic-Durrant, and A. Graser. A robust markerless vision-based human gait analysis system. In *Applied Computational Intelligence and Informatics (SACI), 2011 6th IEEE International Symposium on*, pages 415–420, May 2011.

[14] Ross A Clark, Kelly J Bower, Benjamin F Mentiplay, Kade Paterson, and Yong-Hao Pua. Concurrent validity of the microsoft kinect for assessment of spatiotemporal gait variables. *Journal of biomechanics*, 46(15) :2722–2725, 2013.

[15] Antoine Moevus, Max Mignotte, Jacques A de Guise, and Jean Meunier. A perceptual map for gait symmetry quantification and pathology detection. *Biomedical engineering online (BMEO)*, 14(1) :99, October 2015.

[16] Fabian Pedregosa, Gaël Varoquaux, Alexandre Gramfort, Vincent Michel, Bertrand Thirion, Olivier Grisel, Mathieu Blondel, Peter Prettenhofer, Ron Weiss, Vincent

Dubourg, Jake Vanderplas, Alexandre Passos, David Cournapeau, Matthieu Brucher, Matthieu Perrot, and Édouard Duchesnay. Scikit-learn : Machine learning in python. *The Journal of Machine Learning Research*, 12 :2825–2830, 2011.

Appendix : Algorithm

Estimation of the Asymmetry Indexes

I	Thresholded high frequency spectral energy map (size : $height \times width$) of the depth signal of each pixel at lower limb (Input)
AI_j	Asymmetry indexes of I ($j \in \{1,2,3\}$) (Output)
r	Size of the search interval
G_I	Gradient magnitude map of I
Vct	Vector of floats of size *height*
x_{sym}	Column coordinate estimation of the longitudinal axis

Initialization : $G_I \leftarrow$ gradient magnitude map of I

1. Longitudinal Axis Estimation

▷ **for** *each* $i \in [0,\ldots,height]$ **do**

- grdMax $\leftarrow 0$

  for *each* $j \in [(width/2)-r,\ldots,(width/2)+r]$ **do**

    for *each* $m \in [0,\ldots,width/2]$ **do**

      grd $\leftarrow G_I[i][j-m]+G_I[i][j+m]$

      if (grd $>$ grdMax) { pos $\leftarrow j$ grdMax $\leftarrow$ grd }

  Vct$[i] \leftarrow$ pos

▷ $x_{\text{sym}} \leftarrow$ median value of the vector elements Vct[]

2. Estimation of the Asymmetry Indexes

• $L,R \leftarrow$ Number of pixels located to the left (for L) and to the right (for R) of x_{sym} with a non-zero value

▷ $AI_1 \leftarrow \frac{L}{L+R}$ $AI_2 \leftarrow \frac{R}{L+R}$ $AI_3 \leftarrow \frac{2L}{R}$

CHAPITRE 4

PERIODICITY IRREGULARITY MAP ESTIMATION OF HUMAN GAIT WITH A DEPTH CAMERA FOR PATHOLOGIES DETECTION

Ce chapitre présente notre article soumis pour publication dans la revue "IEEE Journal of Biomedical and Health Informatics". Il est exposé ici dans la langue dans laquelle nous l'avons soumis. Les auteurs sont Didier Ndayikengurukiye et Max Mignotte.

Periodicity Irregularity Map Estimation of Human Gait with a Depth Camera for Pathologies Detection

Didier Ndayikengurukiye and Max Mignotte

abstract

This paper describes a computer vision system based on a depth camera (Microsoft Kinect^{TM}) and a conventional treadmill for a fast and reliable visual detection and analysis of the patient's body parts that have an irregular movement pattern, in terms of periodicity, during walking. In this work, we thus assume that the gait of a healthy subject exhibits anywhere in the human body, during the walking cycles, a depth signal (depending on time and collected by a Kinect^{TM} sensor) with a periodic pattern without noise. Herein, the presence of noise and its importance can be used either as a good indicator of possible pathology in an early (and fast) diagnostic tool or to provide information about the presence and extent of disease or (orthopedic, muscular or neurological) problems in the patient. The depth videos used show, for each one, the gait cycles of either a healthy individual or simulating an orthopedic problem (with the presence of a heel under the right or left foot). The proposed system is able to estimate, from each video sequence, a saliency color map showing the areas of strong gait irregularities, in terms of periodicity (also called aperiodic noise energy), of each subject. Even if the maps obtained are informative and highly discriminant for a direct visual classification, even

for a non-specialist, the proposed system, based on the extraction/classification of features from each obtained map allow us to automatically detect maps representing healthy individuals and those representing individuals with orthopedic problems.

4.1 Introduction

The interest in human motion already existed in classical antiquity and depending on needs and tools available, its study has been progressing over the years [1]. As stated by Rose and Gamble [2], even if human walking is seemingly simple, it remains a complex activity (involving balance, timing and coordination of sight and the other senses) whose complexity is revealed if we try to make its qualitative or quantitative description. Every person walking has characteristics of its own (while also sharing several common characteristics of human gait). This is such a familiar experience that in our life we have recognized, at least one day, a person by his walk. This may explain why some researchers study human gait in perspective of human identification [3–6]. However, the study of human gait has many other areas of application : robotics (e.g., studies on passive dynamic walking), sport sciences [7] (e.g., modeling of athlete motion) [1], video surveillance applications, advanced human computer interfaces or medicine (e.g., rehabilitation technology) etc. Other researches are related to diseases that prevent patients from walking normally [8, 9]. The abnormalities they generate and which may alter the *natural* (bio)mechanics of walking can be classified into five categories : deformity, muscle weakness, sensory loss, pain, and impaired motor control [10].

Most accurate systems, for data acquisition in the study of human movement, are systems with markers [11, 12] but the need for systems without markers also arises [13]. Indeed, these marker-based systems are able to give very accurate but also sparse (and generally not distributed equidistantly) measures over the body. In addition, the high cost of these high-end systems [14] inhibit their widespread usage for routine clinical practices.

In this work, we will focus on how to design and implement a new gait analysis system, from a depth camera placed in front of a subject walking on a conventional tread-

mill, capable of detecting these above-mentioned abnormalities and to quantify their severity and also to localize the different damaged or impaired body parts of the patient. We are also interested in developing a low cost, without markers, non-invasive and simple to set-up, easy to use and fast computer vision based system while being accurate and reliable, for a rapid clinical diagnosis used as a first interesting screening for a possible (orthopedic, muscular or neurological) disease, prior to a more thorough examination by a specialist doctor.

4.2 Previous Work

Most research works on gait analysis (for possible clinical applications) use systems with markers and multiple cameras [15–17]. But other systems, less invasive and less difficult to handle, such as insoles [16, 18], wireless shoes [19], accelerometers [20–22] and Microsoft Kinect^{TM} depth cameras [23, 24] are now also increasingly being used [25].

As proposed herein, the research works introduced in [26] and in [27] also use, for data acquisition, a treadmill and a Microsoft Kinect ^{TM} depth camera. These studies support the hypothesis that a symmetrical gait is generally expected in the case of healthy people. For example, in [26] a depth energy image (DEI) which is, in fact, the pixel-wise mean of all images in the input depth image sequence (over a gait cycle, or a longer period), is first estimated. Then, an abnormal gait is detected from a normal one because a symmetric healthy walk use to generate a DEI exhibiting a symmetric silhouette, in terms of mean depth (energy) and conversely. This two-class detection is then achieved through the measurement of asymmetry indexes, from the DEI. Although, this feasibility study gives good results, it was only tested on 6 subjects. Using the same important concept of gait symmetry in healthy subjects, walking abnormalities are also detected in [27]. In this work, a spatial and temporal registration procedure allows to divide each gait cycle in two sub-cycles (left and right steps) and the comparison between these two sub-cycles, at lower limbs, in term of depth difference, allows to efficiently detect an abnormal gait from a normal one and to also quantify the degree of asymmetry of the lower body. Let us

also mention the system proposed in [28], which is not used for classification (between healthy or unhealthy gait) but that allows to estimate an interesting color map providing a quick overview (in terms of perceptual color difference) of asymmetries existing in the gait cycle of a subject.

In the same spirit, but with a single triaxial accelerometer (providing simultaneous measurements in three orthogonal directions), Moe-Nilssen and Helbostad [29] have estimated human gait parameters like cadence, step length, and measures of gait regularity and symmetry from subjects at free walking speeds.

Contrary to the aforementioned works, our model is not based on asymmetry detection (between left and right lower limbs) as an indicator of possible pathology but rather on the amount of noise altering an *ideal* periodic depth movement of each part of the human body during walking. In our model, we thus assume that the gait of a healthy subject exhibits, anywhere in the human body, during the walking cycles, a depth signal (depending on time and collected a Kinect^{TM} sensor) with a periodic pattern without noise. The proposed system is able to estimate, from each video sequence, a color map visualizing the areas of strong gait irregularities, in terms of periodicity, on the patient's body silhouette. In order to get a reliable estimation of this aperiodic noise energy map we have decided to estimate it, in two fully complementary ways, namely in the temporal and in the frequency domains. This strategy allows us to get two different estimations leading to different estimation errors which can then be efficiently combine in order to improve the classification result in a (complementary) fusion way, in terms of information interaction [30]. This map is clearly informative and highly discriminant for a direct visual classification, even for a non-specialist. Herein, the location and degree of noise (representing the degree of gait irregularities) can be used as a good indicator of possible pathology or to provide information about the presence and extent of medical problems. An automatic system, based on the extraction/classification of features from each obtained map is also proposed and allow us to automatically detect maps representing healthy individuals and those representing individuals with orthopedic problems.

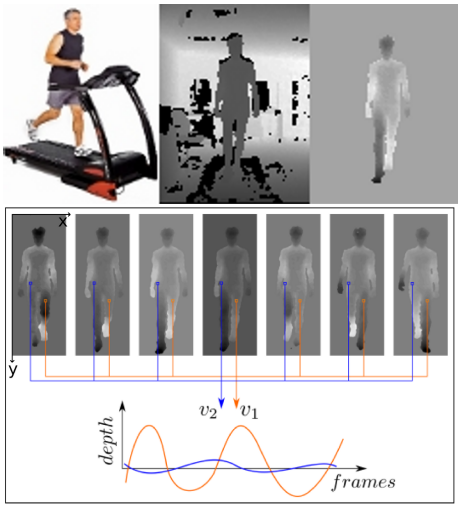

FIGURE 4.1: From lexicographic order ; setup and pre-processing steps with respectively the subject walking on a conventional treadmill (Life Fitness F3), the original depth view recorded from Kinect ^{TM} and the segmented image (after background and treadmill removal). Example of two depth signals (exhibiting a periodic pattern) for a gait cycle of a human subject.

4.3 Proposed Model

The human gait movement is a remarkable example of collaborative interactions between the articular, musculoskeletal and neurological systems working perfectly (and synchronically) together. When everything is working correctly, the healthy loco-motor system produces a smooth, energy efficient, stable gait, exhibiting, at any point of the body, during walking cycles, a (nice) periodic walking pattern without noise. That is why, gait irregularities in terms of periodicity may be a good indicator (and sometimes the first clinical manifestation) of various health problems. In our application, the degree of gait irregularities in terms of periodicity will be also referred, in the following, as being the concept of degree of aperiodicity and quantified by the aperiodic noise energy

since this concept is very close to the one existing and used in speech processing[1].

For this purpose, our system first propose to estimate a saliency color map, providing both an overview of aperiodic noise energy or irregularity energy, in terms of periodicity, existing in the gait cycle of a patient and also capable of showing the areas of strongest gait irregularities. In our application, this map is estimated from the sequence of depth images captured by a Microsoft Kinect^{TM}-style (depth) sensor placed in front of the patient walking[2] on a conventional treadmill.

The Kinect sensor outputs 30 depth maps per second (30 frames per second), with a resolution of 640 per 480 pixels. Each pixel of the depth image cube (or video sequence) is also a 1D depth signal, evolving through time which, in fact, exhibits a periodic walking pattern, without noise, (see Fig. 4.1) for a stable, energy efficient, healthy gait.

Each video sequence shows the gait cycles of a healthy person or the one simulating an orthopedic or muscle disease (presence of a troublesome heel under the right or left foot). More precisely, for the experiments, 17 (healthy) subjects (young male adults, 26.7 ± 3.8 years old, 179.1 ± 11.5 cm height and 75.5 ± 13.6 kg with no reported gait issues) were asked to walk normally on a treadmill (Life Fitness F3) with or without simulated length leg discrepancy (LLD). Every patient had to walk normally (group A), then with a 5 *cm* sole, impairing the normal walk, under the left foot (group B), then with the sole under the right foot (group C). The scene took place in a non-cluttered room where the treadmill is always in the same position relatively to the Kinect ^{TM} camera. In this way, a silhouette extraction strategy (background and treadmill removal) can be easily defined as proposed in [28].

To this end, in order to get a reliable estimation of this 2D spatial map of irregularities

[1] In speech or acoustic signal processing, aperiodic noise is produced by high-frequency (acoustic) energy which is distributed fairly randomly across the upper part of the spectrum. It is distinct from periodic energy, which is associated from acoustic signals such as clearly defined formants of the kind we see in vowels and other sonorants [31]. In other words, the deviations from periodicity of the signal introduce additional components on inharmonic frequencies. The energy on inharmonic frequencies (sometimes normalized by the total energy) provides a good estimation measure of noise aperiodicity [32].

[2] After a habituation period of about 2 min, the walking speed of each subject appeared to become constant and their gait movement is then collected by the Kinect^{TM}.

in periodicity, we have decided to estimate it in two different, and fully complementary ways. The first one is fully (and only) estimated in the temporal domain whereas the second estimation of this map is only performed in the frequency domain. This strategy allows us to get two different estimations, regarding to the aforementioned map of irregularities in periodicity, with respect to two different criteria leading to different estimation errors. In our application, we will see later that these two different estimations could be efficiently combine in order to improve the classification result in a (complementary) fusion way, in terms of information interaction [30].

4.3.1 Estimation of the Aperiodic Noise Energy in the Spatial Domain

To this end, the first step consists in estimating the period T_c of the gait cycle (for each subject) and this can be easily achieved by using the estimation method in the spatial domain described by Cutler and Davis [33]. In this technique, a similarity matrix, comparing all frames of the video sequence, in pairs, is first computed (see Fig. 4.2). More precisely, let F^1 and F^2 be two frames of the video of size $H \times W$. The similarity value between F^1 and F^2, is given by :

$$S_{F^k,F^l} = \sum_{i=1}^{H} \sum_{j=1}^{W} |F^k_{i,j} - F^l_{i,j}| \tag{4.1}$$

and from this squared symmetric similarity matrix S of size $N_i \times N_i$ (with N_i the number of images in the sequence used in the estimation of T_c), its auto-correlation matrix[3] $A(d_x, d_y)$ (see Fig. 4.2) allows us to highlight the peak values that will enable to estimate the gait period T_c :

$$A(d_x, d_y) = \frac{\sum(S_{x,y} - \bar{S})(S_{x+d_x,y+d_y} - \bar{S}_d)}{\sqrt{\sum(S_{x,y} - \bar{S})^2 \sum(S_{x+d_x,y+d_y} - \bar{S}_d)^2}} \tag{4.2}$$

[3] The auto-correlation 2D function is itself periodic with the same period as the similarity matrix (or the video sequence) but has the advantage of being much more robust to noise.

where the different summations are over all pixel locations (x,y) in the image. $\bar{S}$ and $\bar{S}_d$ are respectively the mean of the similarity matrix and the mean of the shifted similarity matrix. d_x and d_y represents respectively the shift relative to the height and width axis.

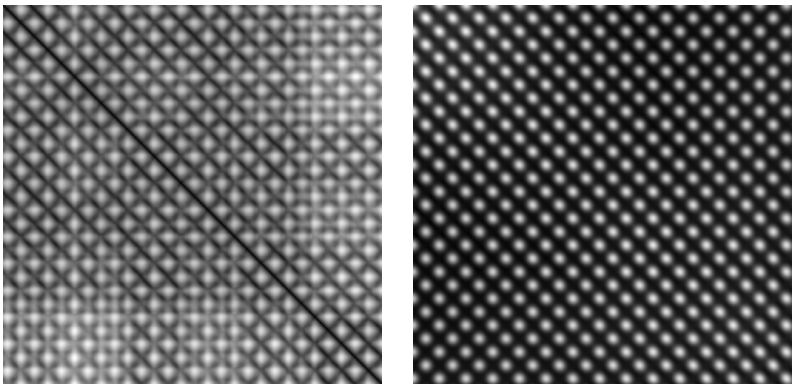

(a) **(b)**

FIGURE 4.2: (a) Images of the similarity matrix S and (b) its auto-correlation function $A(d_x,d_y)$ for the 512 frames of the video and for the $S05_B$ patient (B : with a heel under the left foot).

From the previously estimated gait period T_c, the second step consists of the computation of the noiseless periodic pattern for each depth signal, related to each pixel of the subject silhouette. This step is summarized in Algorithm 2 and is based, in fact, on the simple averaging, in the time domain, of multiple and (non-overlapping) consecutive segments of the depth signal of length T_c. In this context, it is well known that appropriate averaging can increase the Signal to Noise Ratio (SNR), especially for Gaussian noise processes. In the later case, averaging N samples will reduce the mean root mean square (rms) current noise by a factor of $\sqrt{N}$, or the mean noise power by a factor of $1/N$ [34].

The final step is to compute, for each pixel of the subject silhouette, the difference between the original (noised) depth signal and its related noiseless periodic pattern (modulo T_c). This difference signal represents the noise signal $n(x)$ of each depth signal which is then squared integrated over $T \gg T_c$ in order to compute the (temporal) energy

of this noise (see Algorithm 2) :

$$\text{Energy}_{\text{spatial}} = \int_0^T \|n(x)\|^2 \mathrm{d}x \tag{4.3}$$

Each estimated noise energy value, related to each pixel of the subject silhouette, represents thus, in our application, the amount of gait irregularities, in terms of periodicity, of each depth signal, or equivalently (since the treadmill and the depth camera remains fixed during the gait), of each body part of the subject during his gait cycle[4]. This map is also capable of showing the areas of strongest gait irregularities. In our application, this map is visualized in pseudo-color using the thermal scale (from dark blue-cold to red for white spot) in order to make some details more visible (see Fig. 4.3 and 4.4).

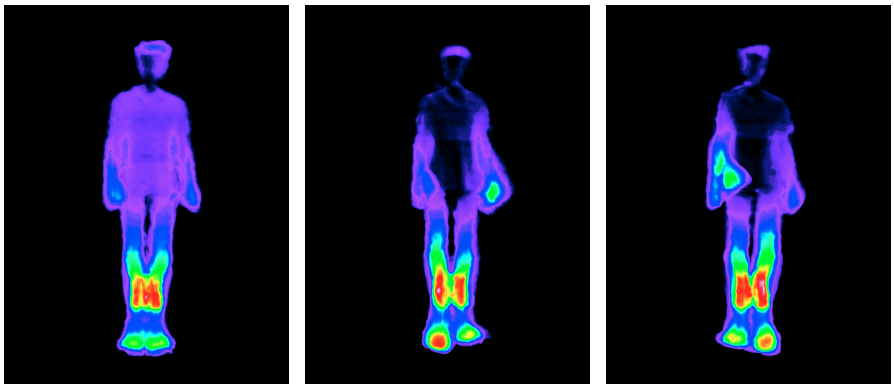

(a) **(b)** **(c)**

FIGURE 4.3: Periodicity irregularity maps for S05 subject (map obtained in the spatial domain). From left to right : (a) Without a heel (b) Heel under left foot (c) Heel under right foot.

[4] Note that the human being makes a translational forward movement as well as lateral movements of the pelvis, axial rotation of the pelvis, the femur and tibia. However the translational movement is in general the most important in amplitude particularly for the leg, relatively to the lateral movements.

4.3.2 Estimation of the Aperiodic Noise Energy in the Frequency Domain

In order to estimate, in the frequency domain, the noiseless periodic pattern of the depth signal (related to each pixel) we rely on the estimation of the mean periodogram introduced by Welch [35]. This improved estimator of the power spectrum density (PSD) consists of dividing the temporal signal of depth into (possibly) overlapping segments x_b. Each segment is weighted by a smooth (e.g., Hamming or Hanning) window[5] and is then processed by a Discrete Fourier Transform (DFT) in order to obtain the modified periodogram $|X_b(\nu)|^2$. The averaging of these modified periodograms allows us to estimate the Welch's PSD estimate [35] $|X_W(\nu)|^2$. This averaging (of modified periodograms) tends to decrease the variance of the PSD estimate relative to a single periodogram estimate of the entire data record. By this fact, the variance is reduced by a factor of L over the periodogram, L being the number of blocks used in the averaging. In our application, we use an overlapping of 50% for segments of length T_s weighted by an Hanning window (and for a length of an entire data record $T = 512$). In addition, we found that the classification rate is also improving as the length T_s decreases until the value $T_s = 16$ (see Fig. 4.5). This gives us a total number of $L = 63$ block segments (used in the averaging) leading to a PSD estimate with a variance reduced by $L = 63$ compared to single periodogram estimation.

The integration of the difference between the Welch's mean periodogram $|X_W(\nu)|^2$ (of length $T_s = 16$) and the periodogram of each $|X_b(\nu)|^2$ allows us to give an estimation, in the frequency domain, of the irregularities in terms of periodicity or the degree of aperiodicity (the so-called aperiodic noise energy) existing in each depth signal.

[5] The windowing suppress the discontinuity, and the resulting spurious high frequencies in the frequency analysis, by "tapering" the recorded signal smoothly to zero at the start and end of the recording period.

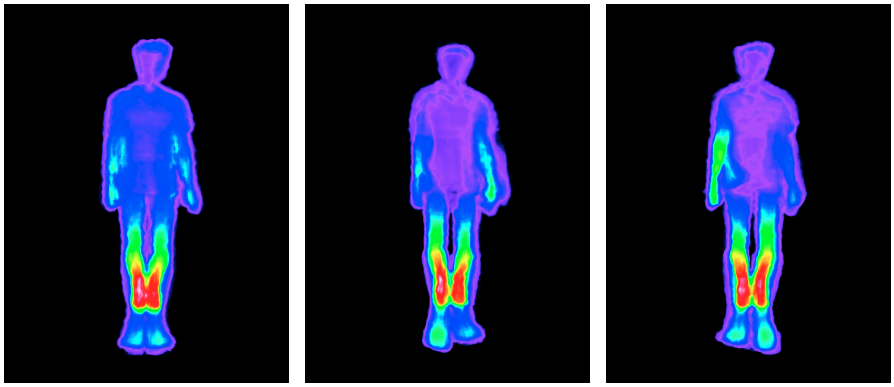

(a) **(b)** **(c)**

FIGURE 4.4: Periodicity irregularity maps for S05 subject (map obtained in the frequency domain). From left to right : (a) Without a heel (b) Heel under left foot (c) Heel under right foot.

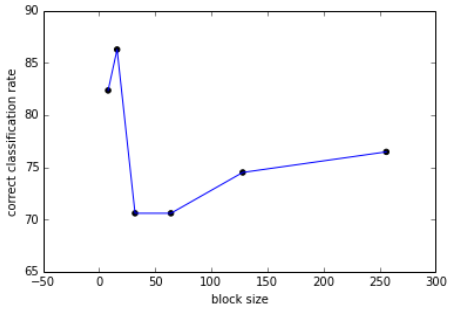

FIGURE 4.5: Curve representing the correct classification rate as a function of the block size.

4.3.3 Automatic Classification of the Subjects

The two maps of aperiodic noise energy, estimated in the frequency and spatial domain, contain the same information but are degraded with different estimation errors. More precisely, these estimation errors are mainly due, in the spatial domain, to the estimation of the period T_c (of the gait cycle) from the autocorrelation of the similarity

matrix and mainly due, in the frequency domain, both to the choice of the window (or apodization) function which slightly modified the spectrum (causing leakage[6]) and the window size $T_s < T$ which reduced the frequency resolution of the spectrum and consequently, bias the amplitudes and shape of the spectrum.

At this stage the estimated maps are highly discriminant for a direct visual classification by the clinician (which can also easily localize the problematic or aperiodic noise parts of the patient's body), or even for a non-specialist (see Figures 4.3 and 4.4). Nevertheless, in order to propose a fully automated gait analysis system, we have also developed a classification scheme based on the extraction of the following features obtained from each obtained map. We classified the maps into two classes, namely healthy individuals and those representing individuals with orthopedic problems (with the left or right foot) and three classes (subject without heel under foot, with heel under left foot, with heel under the right foot).

[6] Different types of windows will have different leakage-properties.

(I)

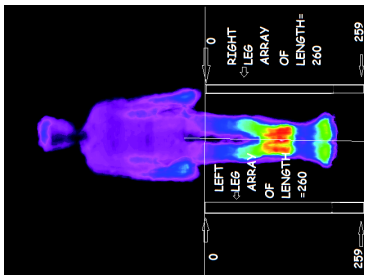

(II)

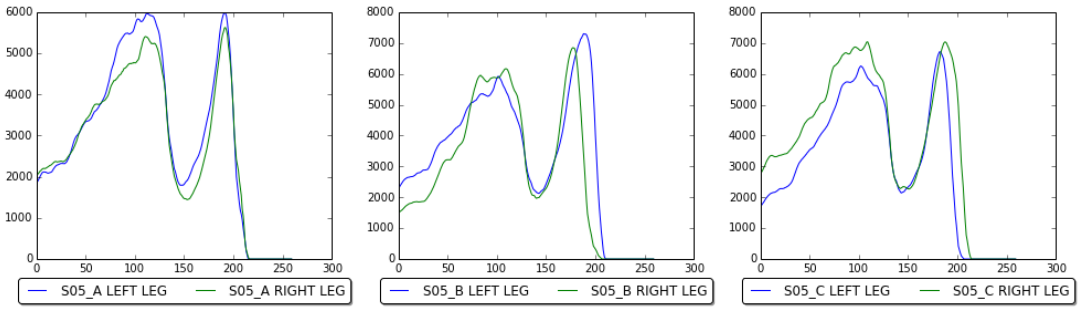

(a) **(b)** **(c)**

FIGURE 4.6: (I)The two vectors of the horizontal summations of the aperiodic noise energy for different values of height of the left and the right leg (from the top of the leg to the bottom of the map), for $S05_A$ subject. (II) Curves (in spatial domain) representing the two vectors of the horizontal summations of the aperiodic noise energy for different values of height of the left and the right leg, as described in (I), for $S05$ subject : (a) Without heel, (b) Heel under left foot, (c) Heel under right foot.

4.3.3.1 Feature Extraction Step :

These features are divided into two major categories. The first group estimates the degree of difference of the aperiodicity noise energy level (or degree of irregularity, in terms of periodicity) between the left and the right leg for each individual and for a height at a given vertical position (see algorithm 4). In fact, it is expected that there is a larger concentration of aperiodic noise energy on the side with the (simulated orthopedic) problem comparatively to the other side. In order to exploit this discriminant property, the horizontal summations of the aperiodic energy values, for different values of height,

from top to bottom of the left and the right leg, are stored in two different vectors for each individual.

This interesting feature is shown by the curves that display the aforementioned vectors for a subject with or without simulated length leg discrepancy (see Fig. 4.6). The figure shows that for subjects without heel under the foot, the curves are almost identical, but the difference is very remarkable for subjects with heel. This suggests that this difference of aperiodic noise energy (for the left and the right leg) provides an interesting and a discriminant feature vector for classification.

The second group of features is related to the deformation or the shape of the silhouette generated by the walking action in the video sequence (and thus is not directly related to the aforementioned concept of aperiodic noise energy). Indeed, the presence of problems or pain in lower limbs (or in the body in general) may disrupt the body's alignment and posture. More precisely, for an healthy gait, the right arm swings in the same direction as the left leg, and conversely with a certain symmetry, in terms of arm and leg swings and approximating, in fact, a (regular and periodical) symmetrical pendular movement.
In order to now model the potential disruption related to a possible asymmetry between the left arm and right leg and vice-versa, we consider the following operations :

1. From the silhouette (given by the set of non-zero values of the) aperiodic noise energy map I (see Fig. 4.7.(a)), we estimate the silhouette asymmetry AS(I), by a simple logical "exclusive or" operation between the left and right part (and conversely) of the binary silhouette (around the preliminary estimated longitudinal axis x_{sym}) (see Algorithm 2 and Fig. 4.7.(c)).

2. We divide the silhouette (see Fig. 4.7.(a)) into two parts (the lower limbs and the upper part of the body above the lower limbs). Each part is then further divided into two sub-parts (the left and the right parts of the longitudinal axis) for a total of four parts (P_1, P_2, P_3 and P_4) (see Fig. 4.7.(b)).

   On these four parts, we compute SURF_1 and SURF_2, the number of pixels (or

surface areas) located, above the lower limbs, respectively, to the left and to the right of x_{sym} on AS(I). We also compute SURF_3 and SURF_4, the number of pixels located, for the lower limbs, respectively, to the left and to the right of x_{sym} on AS(I) (see Fig. 4.7.(c)).

Concretely, the parameters SURF_i represent (in terms of number of pixels), the asymmetry degree (or magnitude) of the facial silhouette between the right and left parts of the body during consecutive gait cycles.

3. We now compute SIL_1 and SIL_2, the two parameters estimated, in the following way :

$$\text{SIL}_1 = 2 \times (\text{SURF}_1 + \text{SURF}_4) \tag{4.4}$$

$$\text{SIL}_2 = 2 \times (\text{SURF}_2 + \text{SURF}_3) \tag{4.5}$$

Concretely speaking, the parameters $\text{SIL}_{1,2}$ represent, the degree or magnitude of asymmetry swing between the left arm and the right leg and vice-versa during gait.

4. In addition, we estimate the following two features :

$$\text{Feat}_2 = \frac{(\text{SIL}_1 - \text{SIL}_2)}{\text{SIL}_1} \text{ if } (\text{SIL}_1 > \text{SIL}_2) \tag{4.6}$$

$$\text{or : } \quad \text{Feat}_2 = \frac{(\text{SIL}_2 - \text{SIL}_1)}{\text{SIL}_2} \text{ if } (\text{SIL}_2 > \text{SIL}_1) \tag{4.7}$$

Finally, Feat_2 quantify the maximum amplitude, in terms of number of pixels, of irregularity, or asymmetry existing in the left arm swing and right leg movement (or conversely) during consecutive gait cycles (or the asymmetric arm and leg swings motion). We multiply the feature value Feat_2 by 1000 in order to equal weight its importance relatively to the first feature vector related to the asymmetry of the aperiodic noise energy (see algorithm 4).

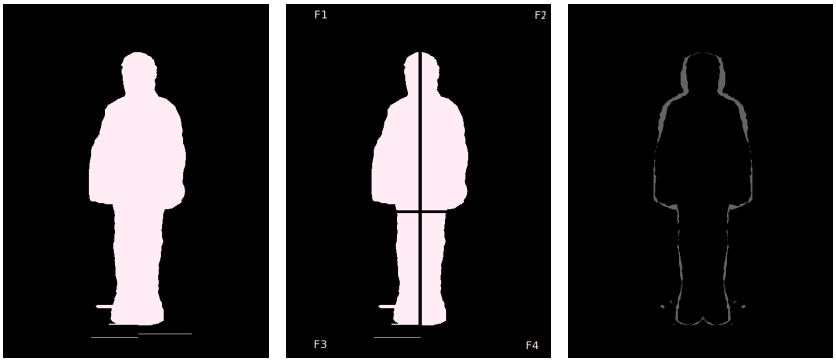

(a) **(b)** **(c)**

FIGURE 4.7: Estimation of AS(I), the (asymmetry) deformation of the silhouette of the aperiodic energy map I (subject $S17_A$). From left to right. (a) The silhouette (defined by the set of non-zero values of aperiodic noise energy I) on either side of the preliminary estimated longitudinal axis x_{sym} (see Algorithm 2). (b) The silhouette divided into four parts : P_1, P_2, P_3 and P_4. (c) Estimation of the silhouette asymmetry AS(I), between the left and right part of the silhouette (given by a simple logical "exclusive or" operation between the left and right part of the binary silhouette and then symmetrized around the longitudinal axis x_{sym}).

4.4 Experimental Results

In our application, the depth of the video cube, to be processed is $T = 512$, which corresponds to a gait video sequence of about 17 seconds (for a Kinect capturing 30 frame per second).

First, concerning the estimation of the aperiodic noise energy in the spatial domain, we can notice on the similarity matrix (see Fig. 4.2) a dark line on the diagonal, that emphasizes the fact that each frame of the video is similar to itself, and also a periodic pattern identical in the vertical and horizontal direction, showing that the human gait exhibits a clear periodic motion [33]. The auto-correlation function of the similarity matrix (see Fig. 4.2) is itself periodic with the same period T_c as the similarity matrix

(or the video sequence) but has the important advantage of being much more robust to noise since each value of the auto-correlation function results from the integration over all values of the similarity matrix. The period T_c of the gait cycle is, of course, slightly different for each subject, but remains about 36 ± 4. Consequently, the estimation of the noiseless periodic pattern of each depth signal (related to each pixel of the subject silhouette and required in the estimation of the aperiodic noise energy map in the spatial domain, see Section 4.3.1), is based on the averaging of $T/T_c \approx 14.22$ depth signals which thus leads to a periodic pattern altered by a mean noise power approximately reduced by a factor around 15 (or a periodic pattern with less than $100/14.22 \approx 7\%$ of aperiodic (irregularity) energy.

Second, concerning the estimation of the aperiodic noise energy in the frequency domain, we recall that we use an overlapping of 50% for segments of length $T_s = 16$, weighted by an Hanning window, for a total of $L = 63$ block segments, used in the averaging, and leading to a PSD estimate with a variance reduced by $L = 63$ compared to single periodogram estimation.

The examples shown in Fig. 4.6, 4.8 and 4.9 confirm that the difference of aperiodicity curves along with the parameter quantifying the asymmetric arm and leg swings motion provide complementary and relevant features for our classification problem.

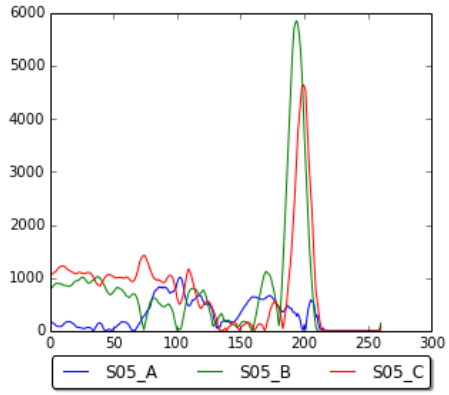

FIGURE 4.8: Curves (in spatial domain) representing the absolute value of the difference of the two vectors of the horizontal summations of the aperiodic noise energy for different values of height, of the left and right leg (as described by Fig.4.6), of the subject $S05$, for the three considered cases, namely ; $S05_A$: subject without the heel ; $S05_B$: subject with the heel under the left foot ; $S05_C$: subject $S05$ with the heel under the right foot.

(a) **(b)** **(c)**

FIGURE 4.9: Silhouette deformation maps for the $S06$ subject. From left to right ; (a) without heel (b) heel under the left foot (c) heel under the right foot.

TABLE 4.1: Classification success rate of 51 periodicity irregularity maps of 17 subjects into two classes (normal or not) (LOOCV : Leave One Out Cross-Validation, LR : Logistic Regression, SVM : Support Vector Machine, k-NN : k-Nearest Neighbors, GNB : Gaussian Naive Bayes, SGDC : Stochastic Gradient Descent Classifier.
PCA : Principal Component Analysis)

SPATIAL DOMAIN	
LOOCV with :	**Success rate :**
k-NN with scaling	90.20%
SVM (kernel :RBF) with scaling	88.23%
GNB with PCA processing	84.31%
LR with scaling	82.35%

SPECTRAL DOMAIN	
LOOCV with :	**Success rate :**
SVM(kernel :polynomial) with PCA preprocessing	86.27%
SVM (kernel :RBF) with scaling	84.31%
GNB with PCA preprocessing	82.35%

MAJORITY VOTING	
LOOCV with :	**Success rate :**
k-NN (spatial), SVM(kernel :RBF) (spatial), SVM(kernel :RBF)(spectral) with scaling	94.12%
SVM (kernel :linear)(spatial), k-NN(spectral), LR(spectral) with scaling	90.20%
k-NN (spatial), k-NN(spectral),k-NN (spatial), k-NN(spectral), SVM(kernel :polynomial)(spectral) with PCA preprocessing	88.23%

TABLE 4.2: Classification success rate of 51 periodicity irregularity maps of 17 subjects into three classes (A : without heel under foot, B : with heel under left foot, C : with heel under right foot) with the same classifiers and data processing like above classification. linSVM mentioned here is a SVM with linear kernel but implemented in a different way than the other SVM (linear).

SPATIAL DOMAIN	
LOOCV with :	**Success rate :**
SVM (linSVM) with scaling	68.62%
LR with PCA processing	64.70%
SVM (kernel :polynomial) without preprocessing	60.78%

SPECTRAL DOMAIN	
LOOCV with :	**Success rate :**
SVM(kernel :linear) with PCA preprocessing	66.66%
LR with PCA preprocessing	64.70%
SGDC with PCA preprocessing	60.78%

The automatic classification of the subjects walking on the treadmill is studied through Gaussian Naive Bayes (GNB), k-Nearest Neighbors (k-NN), Logistic Regression (LR), Support Vector Machine (SVM) and Stochastic Gradient Descent (SGDC) classifiers from the Python's scikit-learn library [36]. The 51 examples are randomly ordered and we use the cross-validation (leave one cross-validation) technique because we have relatively small data set (51 examples). The kernel for SVM with the best rates for two classes is the radial basis function (rbf kernel). For the ternary (*i.e.*, three classes) classification problem, it is the cubic polynomial kernel that gave the best rates.

The classification results into two or three classes are respectively shown in Table 4.1 and Table 4.2 both for individual state-of-the-art classification model used in the literature and exploiting the features extracted from either our aperiodic energy map obtained

in the temporal domain (superscript with a star) or in the frequency domain (superscript with two stars). and also for a simple multiple classifier system whose decisions are then combined through the combination of the estimates obtained from each individual base classifier with the simple majority voting decision rule. The experiments have been tried and tested with or without pre-processing by Principal Component Analysis (PCA) and with or without scaling (the PCA and the scaler are from scikit-learn library [36]).

In addition, we show the classification results into two or three classes with a different fusion strategy (between the feature vector extracted from the aperiodic energy map estimated in the frequency and spectral domains) and consisting simply in concatenating the two feature vectors into a single feature vector (see Table 4.3).

We can also notice that the performance of classifiers to the aperiodic energy maps obtained in the spatial or frequency domains are also somewhat different which in fact makes a multiple classifier based strategy a reliable classification algorithm for our two class classification problem. It also shows that these two maps are complementary and can be effectively combined.

Finally, the results show that the two-class classification problem ("normal" or "abnormal" gait) gives excellent results, especially with a multiple classifier system and the first fusion strategy (see Table 4.1). On the other hand, the three-class classification problem is more complex and the results are disappointing (whatever the fusion strategy used). This can be explained by the fact that the physical behavior of each individual, in terms of response to the presence of a heel (placed below the right or left foot) may be very different across individuals (some of them answer to the problem by a greater oscillation of one arm (or the two arms), or a greater (or smaller or different) stride length, etc.

TABLE 4.3: Classification success rate from features extracted from the periodicity irregularity maps in frequency and spatial domain and placed side by side (51 examples for 17 subjects).
LOOCV : Leave One Out Cross-Validation, LR : Logistic Regression, SVM : Support Vector Machine, k-NN : k-Nearest Neighbors, GNB : Gaussian Naive Bayes and SGDC : Stochastic Gradient Descent Classifier, PCA : Principal Component Analysis ; linSVM mentioned here is a SVM with linear kernel but but implemented in a different way than the other SVM (kernel : linear).

TWO CLASSES	
LOOCV with :	**Success rate :**
k-NN with or without preprocessing	88.23%
GNB with PCA processing	88.23%
SVM (kernel :linear) with PCA processing	84.31%
LR with scaling	84.31%

THREE CLASSES	
LOOCV with :	**Success rate :**
LR with PCA preprocessing	68.62%
k-NN with scaling	66.66%
SVM(linSVM) with scaling	66.66%
SVM (kernel :linear) with scaling	64.70%

4.5 Conclusion

In this work, we have presented a new gait analysis system based on features extracted from the estimation of an aperiodic noise energy map which aims at showing the areas of strong irregularities of the gait, in terms of periodicity, of each subject walking

on a treadmill, and also allows to quantify the degree of asymmetrical (opposite arm and leg) movement patterns. This 2D spatial map is estimated in two complementary ways, namely in the temporal and in the frequency domains in order to get an estimation of the useful information with two different noises and to subsequently provide complementary decisions from different individual classifier which will then be combined. This map also allows for the clinician to visually and quickly localize and quantify the gait abnormalities and for the rehabilitation of patients, to the evolution of these abnormalities over the time. We also hope this system could be useful or a good indicator to quickly detect a possible disease, or for a rapid but reliable diagnosis, prior to a more thorough examination by a specialist doctor. The system proposed in this paper is also inexpensive, marker-less, non-invasive, easy to set up and requiring a small room. These characteristics qualify it for the daily activities in a clinic. This system also makes an automatic classification of healthy patients and those who are unhealthy with good success rates.

BIBLIOGRAPHIE

[1] Reinhard Klette and Garry Tee. Understanding human motion : A historic review. *3d Imaging for Safety and Security*, 1 :22–40, 2007.

[2] Jessica Rose and James Gibson Gamble. *Human walking*. Lippincott Williams & Wilkins Philadelphia, 2006.

[3] Anil Jain, Ruud Bolle, and Sharath Pankanti. *Biometrics : personal identification in networked society*, volume 479. Springer Science & Business Media, 2006.

[4] Davrondzhon Gafurov, Kirsi Helkala, and Torkjel Søndrol. Biometric gait authentication using accelerometer sensor. *Journal of computers*, 1(7) :51–59, 2006.

[5] David Cunado, Mark S Nixon, and John N Carter. Automatic extraction and description of human gait models for recognition purposes. *Computer Vision and Image Understanding*, 90(1) :1–41, 2003.

[6] Rong Zhang, Christian Vogler, and Dimitris Metaxas. Human gait recognition. In *Conference on Computer Vision and Pattern Recognition Workshop, 2004. CVPRW'04.*, pages 18–18. IEEE, 2004.

[7] Christina Strohrmann, Holger Harms, Cornelia Kappeler-Setz, and Gerhard Troster. Monitoring kinematic changes with fatigue in running using body-worn sensors. *IEEE Transactions on Information Technology in Biomedicine*, 16(5) :983–990, 2012.

[8] Luca Palmerini, Laura Rocchi, Sabato Mellone, Franco Valzania, and Lorenzo Chiari. Feature selection for accelerometer-based posture analysis in parkinson's disease. *IEEE Transactions on Information Technology in Biomedicine*, 15(3) :481–490, 2011.

[9] Daniel TH Lai, Pazit Levinger, Rezaul K Begg, Wendy Lynne Gilleard, and Marimuthu Palaniswami. Automatic recognition of gait patterns exhibiting patellofemoral pain syndrome using a support vector machine approach. *IEEE Transactions on Information Technology in Biomedicine*, 13(5) :810–817, 2009.

[10] Jacquelin Perry and Judith M Burnfield. *Gait analysis : normal and pathological function*. Slack Incorporated, 2010.

[11] Marc Bächlin, Meir Plotnik, Daniel Roggen, Inbal Maidan, Jeffrey M Hausdorff, Nir Giladi, and Gerhard Tröster. Wearable assistant for parkinson's disease patients with the freezing of gait symptom. *IEEE Transactions on Information Technology in Biomedicine*, 14(2) :436–446, 2010.

[12] Miikka Ermes, Juha Parkka, Jani Mantyjarvi, and Ilkka Korhonen. Detection of daily activities and sports with wearable sensors in controlled and uncontrolled conditions. *IEEE Transactions on Information Technology in Biomedicine*, 12(1) :20–26, 2008.

[13] Lars Mündermann, Stefano Corazza, and Thomas P Andriacchi. Markerless motion capture for biomechanical applications. In *Human Motion*, pages 377–398. Springer, 2008.

[14] Xin Ma, Haibo Wang, Bingxia Xue, Mingang Zhou, Bing Ji, and Yibin Li. Depth-based human fall detection via shape features and improved extreme learning machine. *IEEE Journal of Biomedical and Health Informatics*, 18(6) :1915–1922, 2014.

[15] Michael W Whittle. Clinical gait analysis : A review. *Human Movement Science*, 15(3) :369–387, 1996.

[16] Adam M Howell, Takehiko Kobayashi, Heather A Hayes, K Bo Foreman, and Stacy JM Bamberg. Kinetic gait analysis using a low-cost insole. *IEEE Transactions on Biomedical Engineering*, 60(12) :3284–3290, 2013.

[17] Motion capture systems from vicon.

[18] Paulo Lopez-Meyer, George D Fulk, and Edward S Sazonov. Automatic detection of temporal gait parameters in poststroke individuals. *IEEE Transactions on Information Technology in Biomedicine*, 15(4) :594–601, 2011.

[19] Stacy J Morris Bamberg, Ari Y Benbasat, Donna Moxley Scarborough, David E Krebs, and Joseph A Paradiso. Gait analysis using a shoe-integrated wireless sensor system. *IEEE Transactions on Information Technology in Biomedicine*, 12(4) :413–423, 2008.

[20] Rolf Moe-Nilssen. A new method for evaluating motor control in gait under real-life environmental conditions. part 1 : The instrument. *Clinical Biomechanics*, 13(4) :320–327, 1998.

[21] Ryo Takeda, Shigeru Tadano, Masahiro Todoh, Manabu Morikawa, Minoru Nakayasu, and Satoshi Yoshinari. Gait analysis using gravitational acceleration measured by wearable sensors. *Journal of biomechanics*, 42(3) :223–233, 2009.

[22] Dean M Karantonis, Michael R Narayanan, Merryn Mathie, Nigel H Lovell, and Branko G Celler. Implementation of a real-time human movement classifier using a triaxial accelerometer for ambulatory monitoring. *IEEE Transactions on Information Technology in Biomedicine*, 10(1) :156–167, 2006.

[23] MJ Landau, BY Choo, and PA Beling. Simulating kinect infrared and depth images. *IEEE transactions on cybernetics*, 2015.

[24] Erik E Stone and Marjorie Skubic. Fall detection in homes of older adults using the microsoft kinect. *IEEE Journal of Biomedical and Health Informatics*, 19(1) :290–301, 2015.

[25] Erik Stone and Marjorie Skubic. Evaluation of an inexpensive depth camera for in-home gait assessment. *Journal of Ambient Intelligence and Smart Environments*, 3(4) :349–361, 2011.

[26] Caroline Rougier, Edouard Auvinet, Jean Meunier, Max Mignotte, and Jacques A de Guise. Depth energy image for gait symmetry quantification. In *Engineering in Medicine and Biology Society, EMBC, 2011 Annual International Conference of the IEEE*, pages 5136–5139. IEEE, 2011.

[27] E. Auvinet, F. Multon, and J. Meunier. Lower limb movement asymmetry measurement with a depth camera. In *Engineering in Medicine and Biology Society (EMBC), 2012 Annual International Conference of the IEEE*, pages 6793–6796, Aug 2012.

[28] Antoine Moevus, Max Mignotte, Jacques A de Guise, and Jean Meunier. A perceptual map for gait symmetry quantification and pathology detection. *Biomedical engineering online (BMEO)*, 14(1) :99, October 2015.

[29] Rolf Moe-Nilssen and Jorunn L Helbostad. Estimation of gait cycle characteristics by trunk accelerometry. *Journal of biomechanics*, 37(1) :121–126, 2004.

[30] Guang-Zhong Yang. *Body Sensor Networks*. Springer-Verlag New York, Inc., Secaucus, NJ, USA, 2006.

[31] P. Backley. *An introduction to element theory*. Edinburgh University Press, 2011.

[32] H Kawahara, J Estill, and O Fujimura. Aperiodicity extraction and control using mixed mode excitation and group delay manipulation for a high quality speech analysis, modification and synthesis system straight. In *Conference MAVEBA*, 2001.

[33] Ross Cutler and Larry S Davis. Robust real-time periodic motion detection, analysis, and applications. *IEEE Transactions on Pattern Analysis and Machine Intelligence*, 22(8) :781–796, 2000.

[34] National Engineering Laboratory (U.S.). Electromagnetic Technology Division. *Optical Fiber Characterization*. Number vol. 1 ;vol. 637 in NBS special publication. U.S. Department of Commerce, National Bureau of Standards, 1982.

[35] P.D. Welch. The use of fast fourier transform for the estimation of power spectra : A method based on time averaging over short, modified periodograms. *IEEE Trans. Audio Electroacoust.*, AU-15 :70–73, 1967.

[36] Fabian Pedregosa, Gaël Varoquaux, Alexandre Gramfort, Vincent Michel, Bertrand Thirion, Olivier Grisel, Mathieu Blondel, Peter Prettenhofer, Ron Weiss, Vincent Dubourg, Jake Vanderplas, Alexandre Passos, David Cournapeau, Matthieu Brucher, Matthieu Perrot, and Édouard Duchesnay. Scikit-learn : Machine learning in python. *The Journal of Machine Learning Research*, 12 :2825–2830, 2011.

Acknowledgment

Ethical approbation was obtained from the research ethics board of our university for this project.

Appendix : Algorithms

Estimation of the longitudinal axis estimation

I Aperiodic noise map (size : $height \times width$) (Input)

x_{sym} Longitudinal axis estimation (Output)

r Size of the search interval

G_I Gradient magnitude map of I

Vct Vector of floats of size *height*

x_{sym} Column coord. estimation of the longitudinal axis

Initialization : $G_I \leftarrow$ gradient magnitude map of I

1. Longitudinal Axis Estimation

▷ **for** *each* $i \in [0, \ldots, height[$ **do**

    grdMx $\leftarrow 0$

    ▷ **for** *each* $j \in [(width/2) - r, \ldots, (width/2) + r[$ **do**

        ▷ **for** *each* $m \in [0, \ldots, width/2[$ **do**

            grd $\leftarrow G_I[i][j-m] + G_I[i][j+m]$

            if (grd $>$ grdMx) { pos $\leftarrow j$ grdMx $\leftarrow$ grd }

    Vct$[i] \leftarrow$ pos

$x_{\text{sym}} \leftarrow$ median value of the vector elements Vct[]

Algorithm 1: Estimation of the longitudinal axis estimation

Estimation of the aperiodic noise energy in the spatial domain

---

s_{depth} Depth signal for each pixel in the subject silhouette (size : $depth$) (Input)

T_c Depth signal period (Input)

n^s_{depth} Aperiodic noise energy of the depth signal (Output)

s_{patt} Noiseless periodic pattern (size : T_c)

c_{patt} Vector containing the number of times that a point of the periodic pattern occurred in the depth signal (size : T_c)

Initialization :

▷ **for** *each* $i \in [0,\ldots,T_c[$ **do**

$s_{patt}[i] \leftarrow 0.0$

$c_{patt}[i] \leftarrow 0$

1. Compute the noiseless periodic pattern

▷ **for** *each* $i \in [0,\ldots,depth[$ **do**

$s_{patt}[i \ modulo \ \mathrm{T}_c] \leftarrow s_{patt}[i \ modulo \ \mathrm{T}_c] + \mathrm{s}_{depth}[\mathrm{i}]$

$c_{patt}[i \ modulo \ \mathrm{T}_c] \leftarrow c_{patt}[i \ modulo \ \mathrm{T}_c] + 1$

▷ **for** *each* $i \in [0,\ldots,T_c[$ **do**

$s_{patt}[i] \leftarrow s_{patt}[i]/c_{patt}[i]$

2. Compute the aperiodic noise energy

$n^s_{\text{depth}} \leftarrow 0$

▷ **for** *each* $i \in [0,\ldots,depth[$ **do**

$n^s_{\text{depth}} += \left(s_{\text{depth}}[i] - s_{patt}[i \ modulo \ T_c]\right)^2$

Algorithm 2: Estimation of the aperiodic noise energy in the spatial domain

Estimation of depth signal noise in frequency domain

using the averaged Welch's periodogram

---

s_{depth} Depth signal in spatial domain (size : $depth$) (Input)

n^f_{depth} Aperiodic noise energy of the depth signal (Output)

b_dim Block dimension (Input) ; h_w Hanning window (size : b_dim)

N_t Temporary vector (size : $depth$) ; n_b Number of blocks

X_{awp} Averaged Welch's periodogram (size : b_dim)

N_{depth} Noise vector in freq. domain (size : $depth$)

x_b A sub-block of s_{depth} in spatial domain (size : b_dim)

Initialization :

$n\_b \leftarrow 0 \quad k \leftarrow 0$

for *each* $i \in [0,\ldots,b\_dim[$ **do**

  $h_w[i] \leftarrow 0.54 - 0.46\cos(2\pi\frac{i}{b\_dim}); X_{awp}[i] \leftarrow 0$

1. Averaged Welch's periodogram estimation

▷**for** *each j = 0 to (depth - b_dim) with j+= b_dim* **do**

  $n\_b \leftarrow n\_b + 1$

  ▷ **for** *each* $i \in [0,\ldots,b\_dim[$ **do**

    $x_b[i] \leftarrow s_{depth}[i+j] \times h_w[i]$

  $X_{mdl} \leftarrow |\text{FFT1D}(x_b)|$

  ▷ **for** *each* $i \in [0,\ldots,b\_dim[$ **do**

    $N_t[k] \leftarrow (X_{mdl}[i])^2; X_{awp}[i] \leftarrow X_{awp}[i] + (X_{mdl}[i])^2; k \leftarrow k+1$

▷ **for** *each j =* $\frac{b\_dim}{2}$ *to (depth -* $\frac{b\_dim}{2}$*) with j+= b_dim* **do**

  $n\_b \leftarrow n\_b + 1$

  ▷ **for** *each* $i \in [0,\ldots,b\_dim[$ **do**

    $x_b[i] \leftarrow s_{depth}[i+j] \times h_w[i]$

  $X_{mdl} \leftarrow |\text{FFT1D}(x_b)|$

  ▷ **for** *each* $i \in [0,\ldots,b\_dim[$ **do**

    $X_{awp}[i] \leftarrow X_{awp}[i] + (X_{mdl}[i])^2$

▷**for** *each* $i \in [0,\ldots,b\_dim[$ **do**

  $X_{awp}[i] \leftarrow \frac{X_{awp}[i]}{n\_b}$

2. Depth signal noise estimation in frequency domain

▷ **for** *each* $i \in [0,\ldots,depth[$ **do**

  $N_{depth}[i] \leftarrow (N_t[i] - X_{awp}[\text{i modulo b\_dim}])$

$n^f_{\text{depth}} \leftarrow 0$

▷ **for** *each* $i \in [0,\ldots,depth[$ **do**

  $n^f_{\text{depth}} += |N_{depth}[i]|$

Algorithm 3: Estimation of the depth signal noise in frequency domain using averaged Welch's periodogram with a 50% overlapping between blocks of size b_dim

Estimation of the features

I Aperiodic noise energy map (size : $height \times width$) (Input)

x_{sym} Longitudinal axis estimation (column coordinate) (Input)

C_l, C_r Vector of the horizontal summation of the aperiodic noise energy for the left (right) area of the longitudinal axis of the lower limbs (size : $height - h$) (Output)

C Vector for the difference of C_l and C_r ; and the value of the silhouette asymmetry (size : $height - h + 1$) (Output)

h Row coord. of the beginning of the lower limbs of I ($h = 380$)

AS(I) Silhouette asymmetry map of I

$\text{SURF}_{1,2,}$ Number of pixels located to the left and to the right of x_{sym} respectively above the lower limbs (on $SA(I)$)

$\text{SURF}_{3,4,}$ Number of pixels located to the left and to the right of x_{sym} respectively for lower limbs part (on $SA(I)$)

1. Computation of vectors C_l, C_r and C

$k \leftarrow 0$

▷ **for** *each* $i \in [h, \ldots, height[$ **do**
  $m_l \leftarrow 0$
  ▷ **for** *each* $j \in [0, \ldots, x_{sym}[$ **do**
    $m_l \leftarrow m_l + I[i][j]$
  $C_l[i-h] \leftarrow m_l; m_r \leftarrow 0$
  ▷ **for** *each* $j \in [x_{sym}, \ldots, width[$ **do**
    $m_r \leftarrow m_r + I[i][j]$
  $C_r[i-h] \leftarrow m_r; C[k] \leftarrow |m_l - m_r|; k \leftarrow k+1$

2. Computation of the silhouette asymmetry features

$x_{\text{sym}} \leftarrow$ Longitudinal axis estimation $[I]$ (cf. Algorithm)
AS(I) $\leftarrow$ "exclusive or" operation around the column coordinate x_{sym} of the binary silhouette I
$\text{SURF}_{1,2,3,4} \leftarrow$ number of pixels located respectively above (right and left) and on the lower limbs
$\text{SIL}_1 \leftarrow 2\ (\text{SURF}_1 + \text{SURF}_4)$

$\text{SIL}_2 \leftarrow 2\ (\text{SURF}_2 + \text{SURF}_3)$
if $(\text{SIL}_1 > \text{SIL}_2)$ C[k] $\leftarrow 1000\ (\text{SIL}_1\text{-SIL}_2)/\text{SIL}_1$
else C[k] $\leftarrow 1000\ (\text{SIL}_2\text{-SIL}_1)/\text{SIL}_2$

Algorithm 4: Estimation of the features

CHAPITRE 5

CONCLUSION

Dans ce travail, nous avons présenté deux nouveaux systèmes d'analyse de la marche humaine. Le premier système se base sur l'estimation d'une carte montrant l'emplacement et l'amplitude de l'énergie de haute fréquence (HFSE) obtenue à partir d'une séquence vidéo de signaux de profondeur pour la marche de chaque individu en expérimentation. Le deuxième système se base aussi sur l'estimation d'une carte mais visualisant la notion d'énergie de bruit apériodique montrant les zones de fortes irrégularités de la marche (en termes de périodicité) et permettant également de quantifier le degré d'asymétrie (la jambe et le bras opposé) de la silhouette durant la marche du sujet en observation. Cette carte spatiale 2D est estimée de deux façons complémentaires, à savoir dans le domaine temporel et dans le domaine fréquentiel, afin d'obtenir une estimation de l'information utile avec deux bruits différents et de fournir ultérieurement aux différents classificateurs des données complémentaires combinées.

Pour ce qui est du classement des sujets à l'étude, le premier système (avec les cartes de HFSE) a un meilleur taux de classement de 92.16% sur tous les 51 individus, 8.82% de faux négatifs et 5.88% de faux positifs. Quant au deuxième système (avec les cartes d'énergie de bruit apériodique), il a un meilleur taux de classement de 90.20% sur tous les 51 individus, 11.76% de faux négatifs et 5.88% de faux positifs. Pour le système avec des cartes de HFSE, nous avons une carte sur 17 (individus sans talonnette) qui est un faux positif, soit la carte de l'individu $S04_A$ (voir Fig.5.1 (a)). Le système avec des cartes d'énergie de bruit apériodique donne aussi sur 17 cartes des individus sans talonnette, la carte de l'individu $S04_A$ comme un faux positif (voir Fig.5.1 (b)). Pour ce qui est des faux négatifs, le premier système présenté en donne 3 : $S07_B$, $S13_B$ et $S14_B$ sur les 34 individus avec talonnette (voir Fig.5.2 (a)) alors que le deuxième système proposé en donne 4 à savoir $S07_B$, $S10_B$, $S13_B$ et $S14_B$ sur les mêmes individus (voir Fig.5.2 (b)).

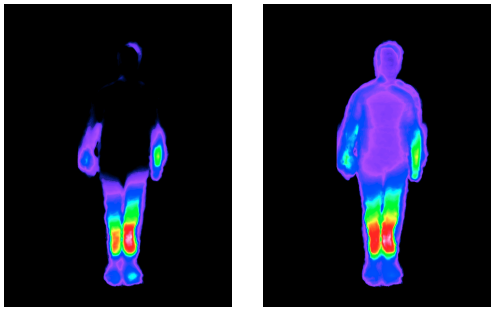

(a) **(b)**

FIGURE 5.1: Carte de l'individu $S04_A$ classé faux positif par les systèmes proposés : (a) le premier système (avec HFSE) (b) le deuxième système (avec l'énergie de bruit apériodique).

Ces deux systèmes génèrent des cartes visuellement proches si on considère surtout la partie problématique représentée par les membres inférieures dans notre cas. De plus, si nous analysons visuellement les cartes des individus mal classés respectivement par le premier et le deuxième système, nous constatons qu'un humain ferait le même classement. En effet, les cartes obtenues par ces systèmes pour l'individu $S04_A$ (faux positif) ressemblent à celles d'individus avec talonnette au pied droit. Pour les cartes des individus classés comme faux négatifs respectivement trois pour le premier et quatre pour le deuxième système, nous constatons que ces cartes sont ceux des individus avec une talonnette au pied gauche (Sujets B). De plus, visuellement, nous constatons qu'un humain les classerait parmi les individus sans talonnette au pied (Sujets A) comme l'a fait le système. Nous estimons donc que chacun de ces systèmes joue bien le rôle de détection des perturbations de la marche et qu'ils sont complémentaires.

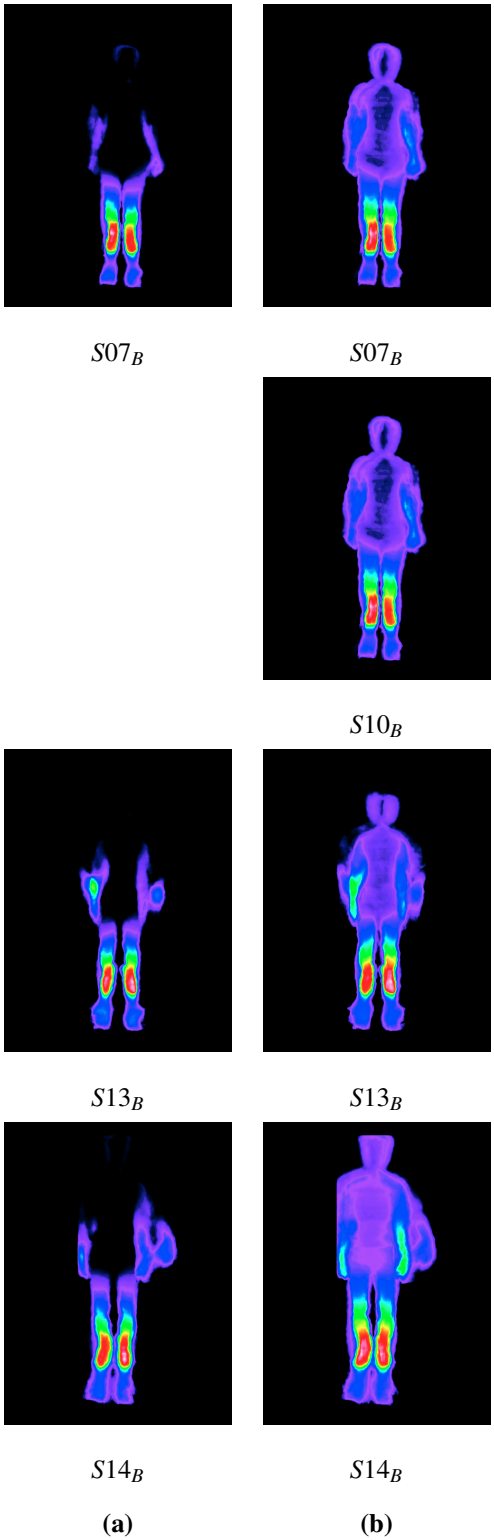

FIGURE 5.2: Cartes d'individus classés faux négatifs par les systèmes proposés : (a) par le premier système (avec HFSE)) (b) par le deuxième système (avec l'énergie de bruit apériodique).

Les cartes obtenues grâce à ces deux systèmes permettraient au clinicien localiser visuellement et de façon rapide les anomalies de la marche, mais aussi de les quantifier. Nous espérons que ces systèmes pourront être utiles comme de bons indicateurs pour détecter rapidement une éventuelle maladie, ou pour un rapide, mais fiable diagnostic, avant un examen plus approfondi par un médecin spécialiste. Les systèmes proposés dans le présent document sont également peu coûteux, sans marqueurs, non invasifs, faciles à installer et nécessitant une petite pièce. Ces caractéristiques les qualifient pour des activités quotidiennes dans une clinique. Lesdits systèmes permettent également une classification automatique des patients en bonne santé et ceux qui ne le sont pas avec de bons taux de succès. Finalement, les méthodes utilisées dans ce travail répondent bien au souhait de Whittle [1] de voir, relativement à l'analyse de la marche, des améliorations dans la facilité et la rapidité avec laquelle les données de la marche peuvent être collectées et interprétées, et une diminution du coût de l'équipement et le niveau de compétence nécessaire pour l'utiliser.

Une extension possible à ce travail est l'amélioration de l'ensemble de données d'analyse en agrandissant sa taille car actuellement elle est constituée de 51 cas de marche répartis en trois ensembles : (Sujets A) 17 cas avec marche normale, (Sujets B) 17 cas avec talonnette sous le pied gauche et (Sujets C) 17 cas avec talonnette sous le pied droit. On pourrait aussi l'enrichir en utilisant d'autres outils incommodants pour la marche de façon que les individus à l'étude puissent manifester des troubles de la marche plus aigus. On pourrait également utiliser des données d'analyse sur de vrais patients avec de vrais problèmes affectant leur marche. Une autre amélioration serait de produire, pour chaque carte, une deuxième qui lui est associée obtenue en utilisant, en plus d'une caméra de profondeur de front, une deuxième caméra de profondeur de profil pour enregistrer les signaux dans le plan transversal parce que pendant la marche, l'être humain effectue un mouvement de translation vers l'avant mais aussi des mouvements latéraux du bassin [2], des rotations axiales du bassin, du fémur, du tibia, etc. [3–5].

BIBLIOGRAPHIE

[1] Michael W Whittle. *Gait analysis : an introduction*. Butterworth-Heinemann, 2007.

[2] Wiebren Zijlstra and At L Hof. Displacement of the pelvis during human walking : experimental data and model predictions. *Gait & posture*, 6(3) :249–262, 1997.

[3] François Plas, Éric Viel, and Yves Blanc. *La marche humaine : kinésiologie dynamique, biomécanique et pathomécanique*. Masson, 1989.

[4] Claudine JC Lamoth, Onno G Meijer, Paul IJM Wuisman, Jaap H van Dieën, Mindy F Levin, and Peter J Beek. Pelvis-thorax coordination in the transverse plane during walking in persons with nonspecific low back pain. *Spine*, 27(4) :E92–E99, 2002.

[5] VP Stokes, C Andersson, and Hm Forssberg. Rotational and translational movement features of the pelvis and thorax during adult human locomotion. *Journal of Biomechanics*, 22(1) :43–50, 1989.

Annexe I

Annexe

TABLE I.1: Sommaire des Algorithmes Utilisés

Estimation de l'axe de symétrie de la silhouette	Algorithme 1
Estimation de l'énergie du bruit apériodique dans le domaine temporel	Algorithme 2
Estimation du bruit du signal de profondeur dans le domaine fréquentiel en utilisant le périodogramme moyenné de Welch avec un chevauchement de 50% entre les blocs	Algorithme 3
Estimation des caractéristiques (attributs) pour les cartes	Algorithme 4

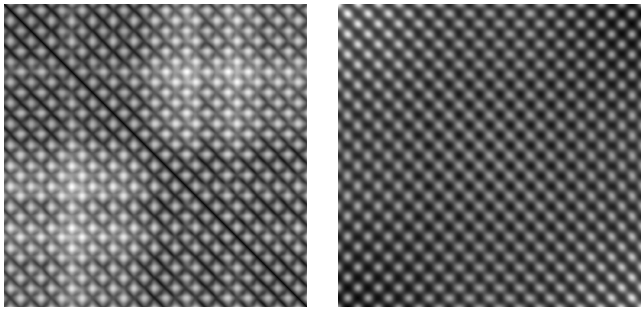

(a) **(b)**

FIGURE I.1: Images de la matrice de similarité S (a) et de sa fonction d'auto-corrélation $A(d_x, d_y)$ (b) pour la séquence vidéo (512 frames) pour l'individu $S12_B$ (B : talonnette sous le pied gauche).

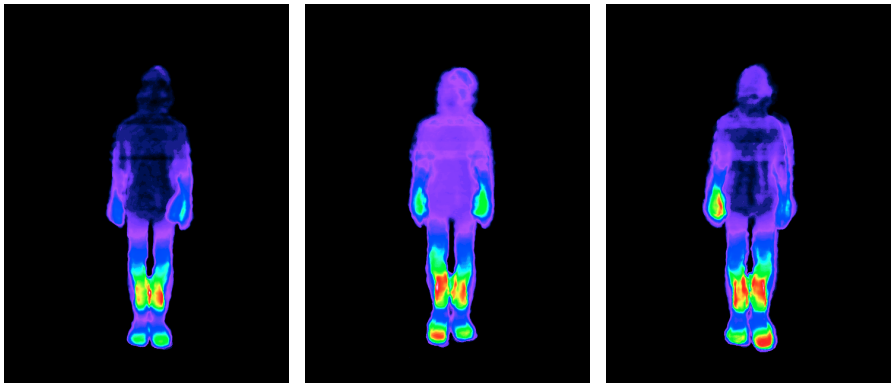

(a) **(b)** **(c)**

FIGURE I.2: Cartes d'irrégularité de périodicité pour l'individu S12 dans le domaine temporel. (a) Sans talonnette (b) Avec une talonnette sous le pied gauche (c) Avec une talonnette sous le pied droit.

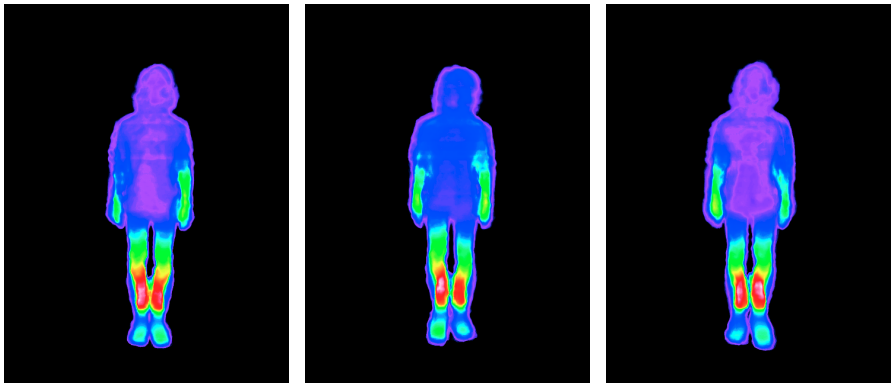

(a) **(b)** **(c)**

FIGURE I.3: Cartes d'irrégularité de périodicité pour l'individu S12 dans le domaine fréquentiel. (a) Sans talonnette (b) Avec une talonnette sous le pied gauche (c) Avec une talonnette sous le pied droit.

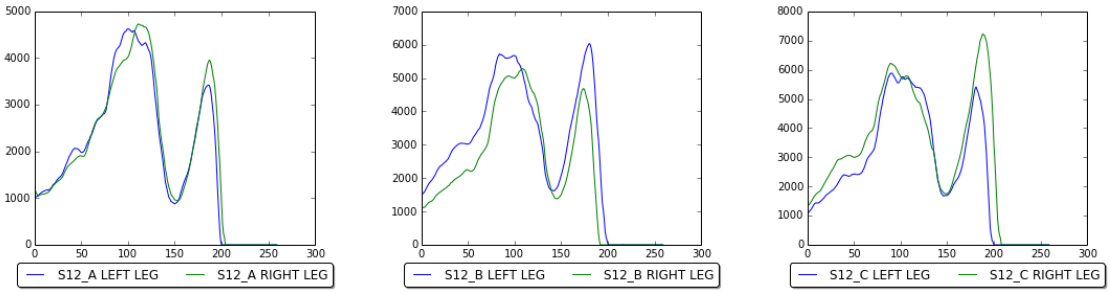

(a) **(b)** **(c)**

FIGURE I.4: Courbes (domaine temporel) représentant les deux vecteurs de la somme de l'énergie du bruit apériodique pour les différentes valeurs de haut en bas pour les pieds droit et gauche, pour l'individu $S12$: (a) Sans talonnette (b) Avec talonnette sous le pied gauche (c) Avec talonnette sous le pied droit.

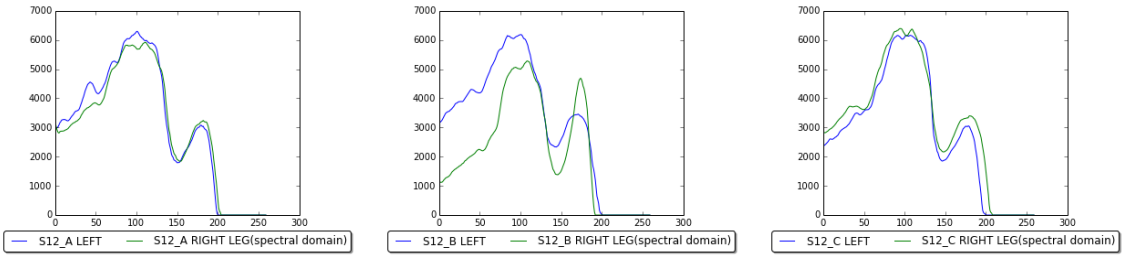

(a) **(b)** **(c)**

FIGURE I.5: Courbes (domaine fréquentiel) représentant les deux vecteurs de la somme de l'énergie du bruit apériodique pour les différentes valeurs de haut en bas pour les pieds droit et gauche, pour l'individu $S12$: (a) Sans talonnette (b) Avec talonnette sous le pied gauche (c) Avec talonnette sous le pied droit.

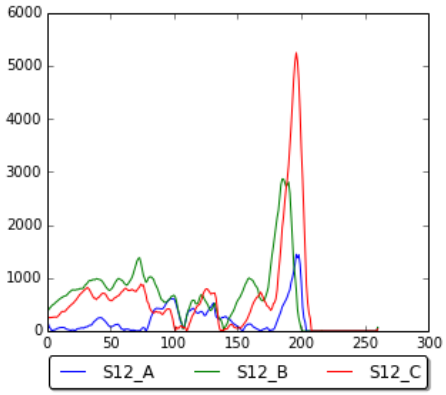

FIGURE I.6: Courbes (domaine temporel) représentant la valeur absolue de la différence des deux vecteurs de la somme de l'énergie du bruit apériodique pour les différentes valeurs de haut en bas pour les pieds droit et gauche, pour l'individu $S12$: (a) Sans talonnette (b) Avec talonnette sous le pied gauche (c) Avec talonnette sous le pied droit.

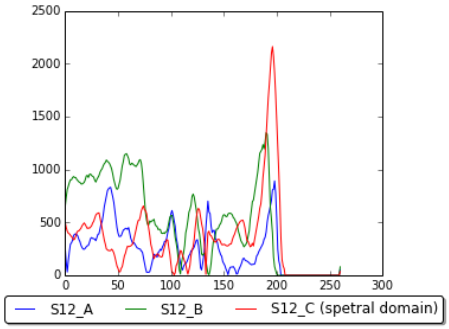

FIGURE I.7: Courbes (domaine fréquentiel) représentant la valeur absolue de la différence des deux vecteurs de la somme de l'énergie du bruit apériodique pour les différentes valeurs de haut en bas pour les pieds droit et gauche, pour l'individu $S12$: (a) Sans talonnette (b) Avec talonnette sous le pied gauche (c) Avec talonnette sous le pied droit.